Kinetic theory analysis of microscale lubrication of a gas between eccentric circular cylinders: Effect of rotation of the outer cylinder

Toshiyuki Doi*

Department of Applied Mathematics and Physics, Faculty of Engineering, Tottori University, Tottori 680-8552, Japan

(Received 8 November 2024; accepted 11 February 2025; published 25 February 2025)

A microscale lubrication flow of a gas between rotating eccentric circular cylinders is studied on the basis of kinetic theory. The dimensionless curvature, defined as the mean clearance divided by the radius of the inner cylinder, is small, the circumferential speeds of the cylinders are small, and the Knudsen number based on the mean clearance is arbitrary. The Boltzmann equation is studied analytically using the slowly varying approximation. A macroscopic lubrication equation is derived, extending the author's previous work [J. Fluid Mech. **974**, A13 (2023)] to include rotation of both cylinders. A direct numerical analysis using the Bhatnagar–Gross–Krook–Welander kinetic model of the Boltzmann equation is conducted to provide a reference solution evaluating the lubrication equation. Two typical problems are examined: (i) comparing the flow of a rotating inner cylinder with that of a rotating outer cylinder at the same speed, and (ii) simultaneous rotation of both cylinders in opposite directions at the same speed. In (i), the difference in the eccentric force between the two flows is small at small Knudsen numbers but becomes significant as the Knudsen number increases. In (ii), the eccentric force nearly vanishes at small Knudsen numbers because of the cancellation of the wedge action due to the opposing rotation; however, considerable eccentric force emerges as the Knudsen number increases. The lubrication equation clarifies these phenomena, attributing them to noncontinuum and curvature effects.

DOI: 10.1103/PhysRevFluids.10.024201

I. INTRODUCTION

Fluid-film lubrication is an important application of fluid dynamics in all technologies involving bodies in relative motion. For lubrication of macroscopic scale, the basic equation known as the Reynolds lubrication equation has been derived from the Navier–Stokes equation [1,2]. However, when the clearance between the bodies is so small that comparable with the mean free path of the gas, lubrication theory based on continuum fluid dynamics is no longer applicable. In such cases, analysis based on kinetic theory is necessary [3]. Theory of microscale lubrication has been studied extensively on the basis of kinetic theory [3–11]. In the 1980s, a generalized lubrication equation that is applicable to an arbitrary Knudsen number was derived [6], where the Knudsen number is defined as the mean free path divided by a reference clearance. A more systematic derivation in given in Ref. [3]. Recently, some attempts have been made to extend the analysis to a system in which an arbitrary temperature difference is present [12–14].

*Contact author: doi@tottori-u.ac.jp

In our previous paper [11], the present author studied a microscale lubrication of a gas between eccentric circular cylinders based on kinetic theory. This is a realistic model of lubrication between a spindle and a bearing in micro-electro-mechanical systems (MEMS). The dimensionless curvature c, defined as the mean clearance divided by the radius of the inner cylinder, was small, and the Knudsen number was arbitrary. The Boltzmann equation has been analytically studied using the slowly varying approximation [3]. One of the important findings in Ref. [11] is that, when the Knudsen number is large, the lubrication performance is affected by the small curvature not by $O(c)$ but rather by $O(\sqrt{c})$. The reason for this phenomenon is as follows. Suppose that the inner cylinder rotates and the outer one is at rest. When the Knudsen number is so large that intermolecular collisions are negligible, the momentum of the gas molecules at an arbitrary point is composed of the momentum that those molecules had when departing one of the cylinders. On the average, the molecules departing from the rotating inner cylinder will have larger circumferential momentum than those departing from the outer cylinder at rest. The key is that, due to the curvature, the number of molecules arriving from the inner cylinder will be smaller than that from the outer cylinder by an amount proportional to $\sqrt{c}$ [10,11]. Therefore, the circumferential momentum in the gas is reduced due to the curvature by $O(\sqrt{c})$. According to lubrication theory, the rise in the gas pressure resulting from the wedge action is proportional to the macroscopic flow velocity induced by the surface motion, i.e., this circumferential momentum. Consequently, the increase in the gas pressure is affected by the curvature by $O(\sqrt{c})$. If we treat a term (say, the curvature term) associated with the curvilinear coordinate as a higher order term in the slowly varying analysis, then the characteristics of the Boltzmann equation will be altered; consequently the difference in the numbers of arriving molecules discussed above will not be evaluated correctly. As a result, a solution so obtained will not approximate the true solution of the Boltzmann equation when the Knudsen number is large. This fact was pointed out and demonstrated in Refs. [10,11]. In Refs. [10,11], an improved lubrication equation was derived through an analysis that correctly evaluates the characteristics of the Boltzmann equation, and its solution was shown to approximate the solution of the Boltzmann equation over the whole range of the Knudsen number.

In Ref. [11], the inner cylinder was rotating and the outer cylinder was at rest. We now consider the opposite flow, in which the outer cylinder rotates and the inner cylinder is at rest. In this case, when the dimensionless curvature c is small, according to continuum lubrication theory, the difference between the two flows is small and at most of $O(c)$. However, when the Knudsen number is large, noting that the number of molecules arriving from the rotating cylinder will now be greater than that from the other cylinder at rest, the difference in the lubrication performance between the two flows may be of $O(\sqrt{c})$ and thus nonnegligible. Note that this phenomenon is not a matter of centrifugal force but is due to noncontinuum effect of molecules arriving from the boundary without collisions.

In this paper, we study a microscale lubrication flow of a gas between eccentric circular cylinders on the basis of kinetic theory. This is an extension of Ref. [11] in that the outer cylinder may now also rotate, and the effect of rotation of this cylinder is studied. The dimensionless curvature is small, the Mach number of the circumferential speed of rotation is small, and the Knudsen number is arbitrary. The Boltzmann equation is analyzed using the slowly varying approximation. A macroscopic lubrication equation which is an extension of Ref. [11] is derived. To assess this, a direct numerical analysis of the Bhatnagar–Gross–Krook–Welander (BGKW) model of the Boltzmann equation [15,16] is also conducted to provide a reference solution. The main goals of this paper are as follows. First, we study the difference between the two flows: one in which only the inner cylinder rotates, and the other in which only the outer cylinder rotates at the same circumferential velocity. We show that a considerable difference in the lubrication performance arises between the two flows when the Knudsen number is large. Second, we study the case of simultaneous rotation, in which both cylinders rotate at the same speed but in opposite directions. According to continuum lubrication theory, the wedge action should almost cancel out due to the opposing rotation, and thus the lubrication force should be at most of $O(c)$. We show that a considerable lubrication force occurs when the Knudsen number is large. Third, we demonstrate that the solution of our lubrication

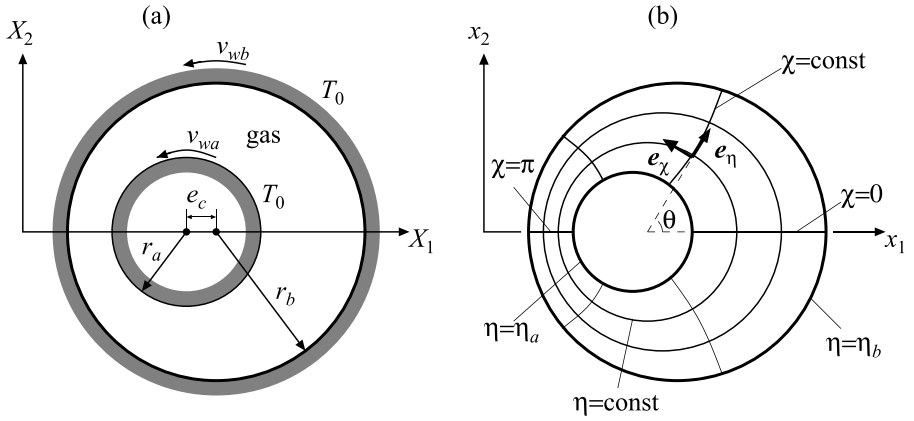

FIG. 1. Schematic of the system. (a) Schematic view of the annulus and (b) the bipolar coordinate system (η, χ) in the dimensionless space.

equation approximates the reference solution over the entire range of the Knudsen number. We also demonstrate that the other lubrication equation, derived from the primitive analysis in which the small curvature term is treated as a higher-order term, produces a solution that qualitatively contradicts the reference solution when the Knudsen number is large.

II. PROBLEM AND BASIC EQUATIONS

A. Problem

Consider a gas in the annulus between eccentric circular cylinders as shown in Fig. 1(a). The radius of the inner cylinder is r_a, that of the outer cylinder is r_b, and the distance between the two axes is e_c. The inner and outer cylinders rotate at constant circumferential velocities v_{wa} and v_{wb}, respectively. The v_{wa} and v_{wb} are positive when the rotation is counterclockwise. For brevity, we refer to "inner rotation" when only the inner cylinder rotates, and "outer rotation" when only the outer cylinder rotates. The temperature of the cylinders is a constant T_0. The dimensionless curvature c is defined by $c = (r_b - r_a)/r_a$. The rarefaction parameter k is defined by $k = (\sqrt{\pi}/2)\ell/(r_b - r_a)$, where ℓ is the mean free path of the gas in the equilibrium state at rest with the average density ρ_0 of the gas and the temperature T_0; we call k the Knudsen number for simplicity. Let c be small, and let the circumferential velocities v_{wa} and v_{wb} of the rotations also be small. The eccentricity $\varepsilon = e_c/(r_b - r_a)$ is arbitrary, but it is not close to unity. To be specific,

$$c \ll 1, \quad \frac{v_{wa}}{(2RT_0)^{1/2}} = \hat{v}_{wa} = cu_{wa}, \quad \frac{v_{wb}}{(2RT_0)^{1/2}} = \hat{v}_{wb} = cu_{wb}, \quad 1 - \varepsilon = O(1), \tag{1}$$

where u_{wa} and u_{wb} are constants of the order of unity, and R is the specific gas constant, i.e., the Boltzmann constant divided by the mass of a molecule. The second and third relations in Eq. (1) imply that the Mach number based on the circumferential velocities v_{wa} or v_{wb} is of the same order as c. The Knudsen number k is arbitrary. We study the time-independent and axially uniform behavior of the gas on the basis of the Boltzmann equation. We also assume that the gas molecules undergo diffuse reflection on the surfaces of the cylinders. Incidentally, an example of the parameters c, ε, and k of an actual microbearing is $c = 0.001$, $\varepsilon = 0.8$, and $k = 0.06$ [17].

B. Basic equation

The dimensionless variables

$$x_i = \frac{X_i}{r_b - r_a}, \quad \zeta_i = \frac{\xi_i}{(2RT_0)^{1/2}} \tag{2}$$

are introduced for the spatial rectangular coordinates X_i and the molecular velocity ξ_i. The dimensionless molecular velocity ζ_i is also denoted by $\boldsymbol{\zeta}$. The dimensionless variable $\hat{f}$ for the velocity distribution function f is defined as

$$\hat{f} = \frac{f}{\rho_0 (2RT_0)^{-3/2}}. \tag{3}$$

In the following analysis, we use the bipolar coordinate system $(\eta, \chi, \zeta_\eta, \zeta_\chi, \zeta_z)$, as shown in Fig. 1(b), defined by

$$x_1 = -\frac{a \sinh \eta}{\cosh \eta - \cos \chi}, \quad x_2 = \frac{a \sin \chi}{\cosh \eta - \cos \chi}, \tag{4}$$

$$\boldsymbol{\zeta} = \zeta_\eta \boldsymbol{e}_\eta + \zeta_\chi \boldsymbol{e}_\chi + \zeta_z \boldsymbol{e}_z, \tag{5}$$

where

$$a = (c\varepsilon)^{-1} \left[(1-\varepsilon^2) \left(1 + c + \frac{1-\varepsilon^2}{4} c^2 \right) \right]^{1/2}. \tag{6}$$

The scale factor h, defined as $h = [(\partial x_1/\partial \eta)^2 + (\partial x_2/\partial \eta)^2]^{1/2} = [(\partial x_1/\partial \chi)^2 + (\partial x_2/\partial \chi)^2]^{1/2}$, is given by

$$h = \frac{a}{\cosh \eta - \cos \chi}. \tag{7}$$

The values of η and χ lie in the ranges $\eta_a \leqslant \eta \leqslant \eta_b$ and $0 \leqslant \chi < 2\pi$, where η_a and η_b are negative constants

$$\eta_a = -\mathrm{arcsinh} ca, \quad \eta_b = -\mathrm{arcsinh} \frac{ca}{1+c}, \quad \eta_a < \eta_b < 0. \tag{8}$$

In Eq. (5), $\boldsymbol{e}_\eta$ and $\boldsymbol{e}_\chi$ are unit vectors in the $x_1 - x_2$ plane normal to the curves $\eta = \text{const}$ and $\chi = \text{const}$, respectively, and $\boldsymbol{e}_z = \boldsymbol{e}_\eta \times \boldsymbol{e}_\chi$. Note that $ca = \varepsilon^{-1}(1-\varepsilon^2)^{1/2} + O(c)$ from Eq. (6).

The dimensionless Boltzmann equation that governs $\hat{f}(\eta, \chi, \zeta_\eta, \zeta_\chi, \zeta_z)$ in the time-independent state for the axially uniform case is written as [18]

$$\frac{\zeta_\eta}{h} \frac{\partial \hat{f}}{\partial \eta} + \frac{\zeta_\chi}{h} \frac{\partial \hat{f}}{\partial \chi} + \frac{1}{h^2} \left(\zeta_\chi \frac{\partial h}{\partial \eta} - \zeta_\eta \frac{\partial h}{\partial \chi} \right) \left(\zeta_\chi \frac{\partial \hat{f}}{\partial \zeta_\eta} - \zeta_\eta \frac{\partial \hat{f}}{\partial \zeta_\chi} \right) = \frac{1}{k} \hat{J}(\hat{f}, \hat{f}). \tag{9}$$

Here, $\hat{J}(\cdot, \cdot)$ is the dimensionless collision integral defined by

$$\hat{J}(\hat{f}, \hat{g}) = \frac{1}{2} \iint [\hat{f}(\boldsymbol{\zeta}_*') \hat{g}(\boldsymbol{\zeta}') + \hat{f}(\boldsymbol{\zeta}') \hat{g}(\boldsymbol{\zeta}_*') - \hat{f}(\boldsymbol{\zeta}_*) \hat{g}(\boldsymbol{\zeta}) - \hat{f}(\boldsymbol{\zeta}) \hat{g}(\boldsymbol{\zeta}_*)] \hat{B} \mathrm{d}\Omega(\boldsymbol{e}) \mathbf{d}\boldsymbol{\zeta}_*,$$

$$\boldsymbol{\zeta}' = \boldsymbol{\zeta} + [\boldsymbol{e} \cdot (\boldsymbol{\zeta}_* - \boldsymbol{\zeta})] \boldsymbol{e}, \quad \boldsymbol{\zeta}_*' = \boldsymbol{\zeta}_* - [\boldsymbol{e} \cdot (\boldsymbol{\zeta}_* - \boldsymbol{\zeta})] \boldsymbol{e}, \tag{10}$$

where $\boldsymbol{e}$ is a unit vector, $\mathrm{d}\Omega(\boldsymbol{e})$ is the solid-angle element in the direction of $\boldsymbol{e}$, and $\mathbf{d}\boldsymbol{\zeta}_* = \mathrm{d}\zeta_{\eta *} \mathrm{d}\zeta_{\chi *} \mathrm{d}\zeta_{z *}$. The $\hat{B}$ is a function of $|\boldsymbol{e} \cdot (\boldsymbol{\zeta}_* - \boldsymbol{\zeta})|/|\boldsymbol{\zeta}_* - \boldsymbol{\zeta}|$ and $|\boldsymbol{\zeta}_* - \boldsymbol{\zeta}|$, and its functional form is determined by the molecular model. In Eq. (10), the arguments of the spatial variables η and χ are common, and they are omitted for simplicity. The integration in Eq. (10) is carried out over the all direction of $\boldsymbol{e}$ and the entire space of $\boldsymbol{\zeta}$. In what follows, the range of integration with respect to $\boldsymbol{\zeta}$ is its whole space unless otherwise stated.

The diffuse-reflection boundary condition on the inner cylinder is given by

$$\hat{f} = \pi^{-3/2} \hat{\sigma}_a \exp\left(-\zeta_\eta^2 - (\zeta_\chi - \hat{v}_{wa})^2 - \zeta_z^2 \right) \quad (\eta = \eta_a, \ \zeta_\eta > 0),$$

$$\hat{\sigma}_a = -2\sqrt{\pi} \int_{\zeta_\eta < 0} \zeta_\eta \hat{f} \mathbf{d}\boldsymbol{\zeta} \quad (\eta = \eta_a). \tag{11}$$

The boundary condition on the outer cylinder is given by

$$\hat{f} = \pi^{-3/2}\hat{\sigma}_b \exp\left(-\zeta_\eta^2 - (\zeta_\chi - \hat{v}_{wb})^2 - \zeta_z^2\right) \quad (\eta = \eta_b,\ \zeta_\eta < 0),$$

$$\hat{\sigma}_b = 2\sqrt{\pi}\int_{\zeta_\eta>0} \zeta_\eta \hat{f}\mathbf{d}\boldsymbol{\zeta}, \quad (\eta = \eta_b). \tag{12}$$

The periodic conditions with respect to χ are given by

$$\hat{f}(\eta, 0, \zeta_\eta, \zeta_\chi, \zeta_z) = \hat{f}(\eta, 2\pi, \zeta_\eta, \zeta_\chi, \zeta_z) \quad (\zeta_\chi > 0), \tag{13}$$

$$\hat{f}(\eta, 2\pi, \zeta_\eta, \zeta_\chi, \zeta_z) = \hat{f}(\eta, 0, \zeta_\eta, \zeta_\chi, \zeta_z) \quad (\zeta_\chi < 0). \tag{14}$$

Note that the boundary condition, including the periodic condition, must be imposed on the molecular velocities pointing into the interior of the domain of interest. Finally, the average gas density ρ_0 is defined by $\iint \mathrm{d}X_1\mathrm{d}X_2 \int f\mathbf{d}\boldsymbol{\xi} = \pi(r_b^2 - r_a^2)\rho_0$, where the spatial integration is conducted over the annular region in Fig. 1(a). In terms of the dimensionless quantities, this equation yields

$$\int_0^{2\pi} \mathrm{d}\chi \int_{\eta_a}^{\eta_b} \mathrm{d}\eta h^2 \int \hat{f}\mathbf{d}\boldsymbol{\zeta} = \frac{2\pi}{c}\left(1 + \frac{c}{2}\right). \tag{15}$$

The macroscopic variables of the gas, i.e., the density ρ, the flow velocity v_i $(i = \eta, \chi)$, the temperature T, the pressure p, and the stress tensor p_{ij} $(i = \eta, \chi; j = \eta, \chi)$, are defined by the moments of the velocity distribution function f. The dimensionless variables $\hat{\rho} = \rho/\rho_0$, $\hat{v}_i = v_i/(2RT_0)^{1/2}$, $\hat{T} = T/T_0$, $\hat{p} = p/p_0$, where $p_0 = R\rho_0 T_0$, and $\hat{p}_{ij} = p_{ij}/p_0$ are given by the moments of the dimensionless distribution function $\hat{f}$ as

$$\hat{\rho} = \int \hat{f}\mathbf{d}\boldsymbol{\zeta}, \tag{16a}$$

$$\hat{v}_i = \frac{1}{\hat{\rho}}\int \zeta_i \hat{f}\mathbf{d}\boldsymbol{\zeta} \quad (i = \chi, \eta), \tag{16b}$$

$$\hat{T} = \frac{2}{3\hat{\rho}}\int \left[(\zeta_\eta - \hat{v}_\eta)^2 + (\zeta_\chi - \hat{v}_\chi)^2 + \zeta_z^2\right]\hat{f}\mathbf{d}\boldsymbol{\zeta}, \tag{16c}$$

$$\hat{p} = \hat{\rho}\hat{T}, \tag{16d}$$

$$\hat{p}_{ij} = 2\int (\zeta_i - \hat{v}_i)(\zeta_j - \hat{v}_j)\hat{f}\mathbf{d}\boldsymbol{\zeta} \quad (i = \eta, \chi; j = \eta, \chi). \tag{16e}$$

Integrating the Boltzmann Eq. (9) over the entire space of ζ_η, ζ_χ, and ζ_z, we obtain the continuity equation:

$$\frac{\partial h\hat{\rho}\hat{v}_\eta}{\partial \eta} + \frac{\partial h\hat{\rho}\hat{v}_\chi}{\partial \chi} = 0. \tag{17}$$

The rectangular components (F_1, F_2) of the force and the torque N acting on the inner cylinder per unit depth are given by

$$\frac{1}{p_0 r_a}\begin{pmatrix} F_1 \\ F_2 \end{pmatrix} = -\int_0^{2\pi} \begin{pmatrix} \hat{p}_{\eta\eta}\cos\theta - \hat{p}_{\chi\eta}\sin\theta \\ \hat{p}_{\eta\eta}\sin\theta + \hat{p}_{\chi\eta}\cos\theta \end{pmatrix} ch\mathrm{d}\chi \quad (\eta = \eta_a), \tag{18}$$

$$\frac{N}{p_0 r_a^2} = -\int_0^{2\pi} \hat{p}_{\chi\eta} ch\mathrm{d}\chi \quad (\eta = \eta_a), \tag{19}$$

where θ is the angle shown in Fig. 1(b), which is defined by

$$\cos\theta = \frac{\cosh\eta\cos\chi - 1}{\cosh\eta - \cos\chi}, \quad \sin\theta = \frac{-\sinh\eta\sin\chi}{\cosh\eta - \cos\chi}. \tag{20}$$

$N > 0$ when the torque is counterclockwise in Fig. 1(a).

The boundary-value problem given by Eqs. (9)–(15) is characterized by the following five dimensionless parameters

$$c = \frac{r_b - r_a}{r_a}, \quad \varepsilon = \frac{e_c}{r_b - r_a}, \quad \hat{v}_{wa} = \frac{v_{wa}}{(2RT_0)^{1/2}}, \quad \hat{v}_{wb} = \frac{v_{wb}}{(2RT_0)^{1/2}}, \quad k = \frac{\sqrt{\pi}}{2}\frac{\ell}{r_b - r_a}. \tag{21}$$

We study this problem under the condition (1).

C. Some transformations

For convenience of the analysis, we introduce the change of independent variables from η, ζ_η, and ζ_χ to y, ζ_ρ, and θ_ζ as follows [21]:

$$\eta = \eta_a + (\eta_b - \eta_a)y, \quad \zeta_\eta = \zeta_\rho \cos\theta_\zeta, \quad \zeta_\chi = \zeta_\rho \sin\theta_\zeta, \tag{22}$$

where $0 \leqslant y \leqslant 1, 0 \leqslant \zeta_\rho < \infty$, and $-\pi < \theta_\zeta \leqslant \pi$. The y in the first relation is the stretched coordinate for η. In terms of the new variables $y, \zeta_\rho, \theta_\zeta, \chi$, and ζ_z, the boundary-value problem Eqs. (9)–(15) is rewritten as follows. The Boltzmann equation is

$$\frac{\zeta_\rho \cos\theta_\zeta}{\gamma H}\frac{\partial \hat{f}}{\partial y} + c\frac{\zeta_\rho \sin\theta_\zeta}{H}\frac{\partial \hat{f}}{\partial \chi} - c\zeta_\rho G\frac{\partial \hat{f}}{\partial \theta_\zeta} = \frac{1}{k}\hat{J}(\hat{f}, \hat{f}), \tag{23}$$

where

$$H = ch = \frac{-\sinh\eta_a}{\cosh\eta - \cos\chi}, \quad G = \frac{-\sinh\eta\sin\theta_\zeta + \sin\chi\cos\theta_\zeta}{-\sinh\eta_a}, \quad \gamma = \frac{\eta_b - \eta_a}{c}. \tag{24}$$

In Eq. (24) and in what follows, η should be understood as $\eta(y)$, as in Eq. (22). Note that H, G, and γ are of $O(1)$. The boundary conditions Eqs. (11)–(14) and the subsidiary condition Eq. (15) are transformed into

$$\hat{f} = \hat{\sigma}_a E \exp\left(2cu_{wa}\zeta_\rho \sin\theta_\zeta - c^2u_{wa}^2\right) \quad (y = 0,\ \cos\theta_\zeta > 0), \tag{25}$$

$$\hat{f} = \hat{\sigma}_b E \exp\left(2cu_{wb}\zeta_\rho \sin\theta_\zeta - c^2u_{wb}^2\right) \quad (y = 1,\ \cos\theta_\zeta < 0), \tag{26}$$

$$\hat{\sigma}_a = -2\sqrt{\pi}\iiint_{\cos\theta_\zeta<0} \zeta_\rho^2 \cos\theta_\zeta \hat{f}\mathrm{d}\zeta_\rho\mathrm{d}\theta_\zeta\mathrm{d}\zeta_z \quad (y = 0),$$

$$\hat{\sigma}_b = 2\sqrt{\pi}\iiint_{\cos\theta_\zeta>0} \zeta_\rho^2 \cos\theta_\zeta \hat{f}\mathrm{d}\zeta_\rho\mathrm{d}\theta_\zeta\mathrm{d}\zeta_z \quad (y = 1),$$

$$\hat{f}(y, 0, \zeta_\rho, \theta_\zeta, \zeta_z) = \hat{f}(y, 2\pi, \zeta_\rho, \theta_\zeta, \zeta_z) \quad (\theta_\zeta > 0), \tag{27}$$

$$\hat{f}(y, 2\pi, \zeta_\rho, \theta_\zeta, \zeta_z) = \hat{f}(y, 0, \zeta_\rho, \theta_\zeta, \zeta_z) \quad (\theta_\zeta < 0), \tag{28}$$

$$\int_0^{2\pi}\mathrm{d}\chi\int_0^1 \mathrm{d}yH^2\iiint \zeta_\rho\hat{f}\mathrm{d}\zeta_\rho\mathrm{d}\theta_\zeta\mathrm{d}\zeta_z = \frac{2\pi}{\gamma}\left(1 + \frac{c}{2}\right), \tag{29}$$

where $E = \pi^{-3/2}\exp(-\zeta_\rho^2 - \zeta_z^2)$. Hereafter, we use the convention that $\hat{f}(\eta(y), \chi, \zeta_\eta(\zeta_\rho, \theta_\zeta), \zeta_\chi(\zeta_\rho, \theta_\zeta), \zeta_z)$ is simply written as $\hat{f}(y, \chi, \zeta_\rho, \theta_\zeta, \zeta_z)$ because no confusion will arise. The ranges of integration with respect to ζ_ρ, θ_ζ, and ζ_z are, respectively, $0 < \zeta_\rho < \infty$, $-\pi < \theta_\zeta < \pi$, and $-\infty < \zeta_z < \infty$ unless otherwise stated.

The macroscopic variables are

$$\hat{\rho} = \iiint \zeta_\rho \hat{f} \mathrm{d}\zeta_\rho \mathrm{d}\theta_\zeta \mathrm{d}\zeta_z, \tag{30a}$$

$$\hat{v}_\eta = \frac{1}{\hat{\rho}} \iiint \zeta_\rho^2 \cos\theta_\zeta \hat{f} \mathrm{d}\zeta_\rho \mathrm{d}\theta_\zeta \mathrm{d}\zeta_z, \tag{30b}$$

$$\hat{v}_\chi = \frac{1}{\hat{\rho}} \iiint \zeta_\rho^2 \sin\theta_\zeta \hat{f} \mathrm{d}\zeta_\rho \mathrm{d}\theta_\zeta \mathrm{d}\zeta_z, \tag{30c}$$

$$\hat{T} = \frac{2}{3\hat{\rho}} \iiint \zeta_\rho \left[(\zeta_\rho \cos\theta_\zeta - \hat{v}_\eta)^2 + (\zeta_\rho \sin\theta_\zeta - \hat{v}_\chi)^2 + \zeta_z^2 \right] \hat{f} \mathrm{d}\zeta_\rho \mathrm{d}\theta_\zeta \mathrm{d}\zeta_z, \tag{30d}$$

$$\hat{p} = \hat{\rho}\hat{T}, \tag{30e}$$

$$\hat{p}_{\eta\eta} = 2 \iiint \zeta_\rho (\zeta_\rho \cos\theta_\zeta - \hat{v}_\eta)^2 \hat{f} \mathrm{d}\zeta_\rho \mathrm{d}\theta_\zeta \mathrm{d}\zeta_z, \tag{30f}$$

$$\hat{p}_{\chi\eta} = \hat{p}_{\eta\chi} = 2 \iiint \zeta_\rho (\zeta_\rho \cos\theta_\zeta - \hat{v}_\eta)(\zeta_\rho \sin\theta_\zeta - \hat{v}_\chi) \hat{f} \mathrm{d}\zeta_\rho \mathrm{d}\theta_\zeta \mathrm{d}\zeta_z. \tag{30g}$$

Changing the variable η into y using Eq. (22), integrating Eq. (17) with respect to y from 0 to 1, and applying the boundary condition Eq. (25) or (26), we obtain the mass conservation equation

$$\frac{\mathrm{d}}{\mathrm{d}\chi} \int_0^1 H \hat{\rho} \hat{v}_\chi \mathrm{d}y = 0. \tag{31}$$

III. ANALYSIS

A. Preliminary remarks

In this section, we analytically study the boundary-value problem (23)–(29) for a small dimensionless curvature c using the slowly varying approximation [3]. This analysis is a straightforward extension of that in Ref. [11] to the present case in which the outer cylinder may also rotate. Thus, only a brief outline is presented here, and more detail is given in Appendix A.

We seek the solution as a power-series expansion in c:

$$\hat{f} = \hat{f}_{(0)} + \hat{f}_{(1)} c + \cdots. \tag{32}$$

Note that the second and third terms in Eq. (23) are multiplied by the small factor c. Thus, substituting the expansion (32) into the boundary-value problem (23)–(29) and formally arranging the terms will yield a series of boundary-value problems for a spatially one-dimensional (1D) Boltzmann equation in which only the derivative $\partial/\partial y$ is involved; other derivatives $\partial/\partial\theta_\zeta$ and $\partial/\partial\chi$ appear as higher-order inhomogeneous terms. Although this approach may appear feasible, the solution obtained fails to approximate that of the Boltzmann equation when the Knudsen number is sufficiently large that $ck^2 \gg 1$. The reason for this discrepancy is explained in the second paragraph in Sec. I. Some examples will be presented in Sec. V, and the further discussion on this primitive approach is left to Sec. III D. In Refs. [10,11], therefore, it was suggested that the third term in Eq. (23), which is specific to the curvilinear coordinate system and may be referred to as the curvature term, should be treated together with the first term regardless of c. To be specific, we define the derivative operator

$$\mathrm{D}'_{\mathrm{ec}} = \frac{\cos\theta_\zeta}{\gamma H} \frac{\partial}{\partial y} - \frac{c \sinh\eta \sin\theta_\zeta}{\sinh\eta_a} \frac{\partial}{\partial\theta_\zeta}. \tag{33}$$

In terms of $\mathrm{D}'_{\mathrm{ec}}$, the Boltzmann Eq. (23) is written as

$$\zeta_\rho \mathrm{D}'_{\mathrm{ec}} \hat{f} + c \frac{\zeta_\rho \sin\chi \cos\theta_\zeta}{\sinh\eta_a} \frac{\partial \hat{f}}{\partial\theta_\zeta} + c \frac{\zeta_\rho \sin\theta_\zeta}{H} \frac{\partial \hat{f}}{\partial\chi} = \frac{1}{k} \hat{J}(\hat{f}, \hat{f}). \tag{34}$$

Here, the second term on the left-hand side is excluded from $\mathrm{D}'_{\mathrm{ec}}\hat{f}$ so that $\mathrm{D}'_{\mathrm{ec}}$ preserves the parity in θ_ζ. This is permissible because the shape of the characteristics is crucial around $\theta_\zeta = \pm\pi/2$ [11] and the excluded term vanishes at $\theta_\zeta = \pm\pi/2$.

The expansion (32) is substituted into Eqs. (25)–(29) and (34), and the terms are arranged assuming

$$\mathrm{D}'_{\mathrm{ec}}\hat{f} = \mathrm{D}'_{\mathrm{ec}}\hat{f}_{(0)} + \mathrm{D}'_{\mathrm{ec}}\hat{f}_{(1)}c + \cdots, \quad \mathrm{D}'_{\mathrm{ec}}\hat{f}_{(m)} = O(\hat{f}_{(m)})\ (m = 0, 1, \cdots). \tag{35}$$

In this way, the projection of the characteristics of Eq. (34) onto the θ_ζ-y plane is preserved. This method was verified to work well over the entire range of the Knudsen number [10,11].

B. Generalized lubrication equation

Following the procedure in Appendix A, the solution up to $\hat{f} = \hat{f}_{(0)} + \hat{f}_{(1)}c$ is written as

$$\hat{f}(y, \chi, \boldsymbol{\zeta}) = \hat{p}_{(0)}E\left\{1 + c\left[\frac{1}{\hat{p}_{(0)}}\frac{\mathrm{d}\hat{p}_{(0)}}{\mathrm{d}\chi}\Phi_{\mathrm{P}}\left(y, \boldsymbol{\zeta}; \frac{k}{\hat{p}_{(0)}}, \chi\right)\right.\right.$$
$$\left.\left. + u_{wa}\Phi_{\mathrm{Ca}}\left(y, \boldsymbol{\zeta}; \frac{k}{\hat{p}_{(0)}}, \chi\right) + u_{wb}\Phi_{\mathrm{Cb}}\left(y, \boldsymbol{\zeta}; \frac{k}{\hat{p}_{(0)}}, \chi\right) + \frac{C_{(1)}}{\hat{p}_{(0)}}\right]\right\}, \tag{36}$$

in terms of the undetermined functions $\hat{p}_{(0)}(\chi)$ and $C_{(1)}(\chi)$, where $\boldsymbol{\zeta}$ is an abbreviation for $(\zeta_\rho, \theta_\zeta, \zeta_z)$. The leading-order solution is a Maxwellian at rest. The first-order solution is a linear combination of the three fundamental flow problems defined, respectively, by Eqs. (A15) and (A16), Eqs. (A17) and (A18), and Eqs. (A19) and (A20). Here, $\Phi_{\mathrm{P}}(y, \boldsymbol{\zeta}; \tilde{k}, \chi)$ is the solution of a flow between the eccentric cylinders at rest induced by a pressure gradient; this flow may be referred to as the generalized Poiseuille flow. The $\Phi_{\mathrm{Ca}}(y, \boldsymbol{\zeta}; \tilde{k}, \chi)$ and $\Phi_{\mathrm{Cb}}(y, \boldsymbol{\zeta}; \tilde{k}, \chi)$ are the solutions of flows between these cylinders induced by a rotation of the inner or the outer cylinder, respectively; these may be referred to as the generalized Couette flows for inner and outer rotation, respectively. The functions Φ_{P} and Φ_{Ca} are identical with Φ_{Pec} and Φ_{Cec} in Ref. [11], respectively. The $\tilde{k}$ is the parameter that stands for $k/\hat{p}_{(0)}$, which is called the local Knudsen number accounting for the variation of the mean free path due to the finite pressure variation. The $\hat{p}_{(0)}$ is the leading term of the expansion $\hat{p} = \hat{p}_{(0)} + \hat{p}_{(1)}c + \cdots$ of the pressure $\hat{p}$ corresponding to Eq. (32), which is an unknown function of χ to be determined later. Once $\hat{p}_{(0)}$ is known, the solution is given by Eq. (36) leaving $C_{(1)}$ undetermined which is determined in the next order analysis, see Appendix B in Ref. [11].

The unknown $\hat{p}_{(0)}$ is determined by conservation of mass. Substituting Eq. (36) into Eq. (30c) and then into Eq. (31), we obtain

$$\frac{\mathrm{d}}{\mathrm{d}\chi}\left[m_{\mathrm{P}}\left(\frac{k}{\hat{p}_{(0)}}, \chi\right)\frac{\mathrm{d}\hat{p}_{(0)}}{\mathrm{d}\chi} + u_{wa}\hat{p}_{(0)}m_{\mathrm{Ca}}\left(\frac{k}{\hat{p}_{(0)}}, \chi\right) + u_{wb}\hat{p}_{(0)}m_{\mathrm{Cb}}\left(\frac{k}{\hat{p}_{(0)}}, \chi\right)\right] = 0. \tag{37}$$

Here, $m_{\mathrm{P}}(\tilde{k}, \chi)$, $m_{\mathrm{Ca}}(\tilde{k}, \chi)$, and $m_{\mathrm{Cb}}(\tilde{k}, \chi)$ are defined by Eq. (A23) in Appendix A as integrals of Φ_{P}, Φ_{Ca}, and Φ_{Cb}, respectively. They are called the flow-rate coefficient of generalized Poiseuille flow and those of Couette flows for inner and outer rotation, respectively. Here, m_{P} and m_{Ca} are, respectively, identical with m_{Pec} and m_{Cec} in Ref. [11]. The solution is constructed as follows. First, let the boundary-value problems (A15)–(A20) be solved for a so wide range of $\tilde{k}$ that a database of the functions m_{P}, m_{Ca}, and m_{Cb} be known. Then, $\hat{p}_{(0)}$ is determined by the ordinary differential Eq. (37) subject to Eq. (29) and the periodic condition (see Appendix B in [11]). Substituting $\hat{p}_{(0)}$ into Eq. (36), the distribution function $\hat{f}$ is obtained. Substituting (36) into (30a)–(30g), the macroscopic variables are obtained. For example, the component $\hat{v}_\chi$ of the flow velocity, the components of the stress tensor, and the pressure $\hat{p}$ up to the nontrivial leading orders are

given by

$$\hat{v}_\chi = c\left[\frac{1}{\hat{p}_{(0)}}\frac{\mathrm{d}\hat{p}_{(0)}}{\mathrm{d}\chi}u_{\mathrm{P}}\left(y;\frac{k}{\hat{p}_{(0)}},\chi\right)+u_{wa}u_{\mathrm{Ca}}\left(y;\frac{k}{\hat{p}_{(0)}},\chi\right)+u_{wb}u_{\mathrm{Cb}}\left(y;\frac{k}{\hat{p}_{(0)}},\chi\right)\right], \tag{38}$$

$$\hat{p}_{\eta\eta} = \hat{p} = \hat{p}_{(0)}, \tag{39}$$

$$\hat{p}_{\chi\eta} = c\left[\frac{\mathrm{d}\hat{p}_{(0)}}{\mathrm{d}\chi}S_{\mathrm{P}}\left(y;\frac{k}{\hat{p}_{(0)}},\chi\right)+u_{wa}\hat{p}_{(0)}S_{\mathrm{Ca}}\left(y;\frac{k}{\hat{p}_{(0)}},\chi\right)+u_{wb}\hat{p}_{(0)}S_{\mathrm{Cb}}\left(y;\frac{k}{\hat{p}_{(0)}},\chi\right)\right], \tag{40}$$

where the functions $u_{\mathrm{P}}(y;\tilde{k},\chi)$, $u_{\mathrm{Ca}}(y;\tilde{k},\chi)$, and $u_{\mathrm{Cb}}(y;\tilde{k},\chi)$ are the normalized flow velocities corresponding to Φ_{P}, Φ_{Ca}, and Φ_{Cb}, respectively, defined by Eq. (A21), and the functions $S_{\mathrm{P}}(y;\tilde{k},\chi)$, $S_{\mathrm{Ca}}(y;\tilde{k},\chi)$, and $S_{\mathrm{Cb}}(y;\tilde{k},\chi)$ are normalized shear stresses defined by Eq. (A22). Substituting Eqs. (39) and (40) into Eq. (18), the eccentric force is obtained. In this construction of the solution, Eq. (37) plays the role of determining the pressure distribution $\hat{p}_{(0)}$. In this sense, Eq. (37) may be referred to as a generalized lubrication equation. The difference from Ref. [11] is the term containing m_{Cb}, which is the contribution from the rotation of the outer cylinder. Equations (A15)–(A20) are boundary-value problems of the spatially 1D Boltzmann equations. Therefore, to solve them is an extremely easier task [11] than solving the full boundary-value problem (23)–(29). Further, by making the database of the functions m_{P}, m_{Ca}, and m_{Cb} beforehand, Eq. (37) is absolutely an ordinary differential equation that can be solved as easily as the conventional 1D Reynolds equation.

Equation (37) is similar to the spatially 1D Reynolds equation derived from the Navier–Stokes equation. The difference is that the factors comprised of the viscosity and the clearance in the latter are replaced by the functions m_{P}, m_{Ca}, and m_{Cb}. Thus, the noncontinuum effects arise through these functions. Therefore, it is natural to examine the properties of these functions prior to actual numerical analyses. This is undertaken in the next subsection. The Reynolds equation derived from the Navier–Stokes equation is given in Appendix B for self-containedness.

C. Flow-rate coefficients

In this subsection, we present the flow-rate coefficients and examine their properties. The function m_{P} for the generalized Poiseuille flow is omitted here, because it has been presented in Ref. [11]. Functions m_{Ca} and m_{Cb} for the BGKW kinetic model are presented in Fig. 2 as functions of the local Knudsen number $\tilde{k}$ and the longitudinal coordinate χ. The main goal of this subsection is to examine the difference between m_{Ca} and m_{Cb}. This difference is small when $\tilde{k}$ is small. However, it becomes significant as $\tilde{k}$ increases. The function m_{Cb} for the outer rotation is greater. The difference also increases with the dimensionless curvature c.

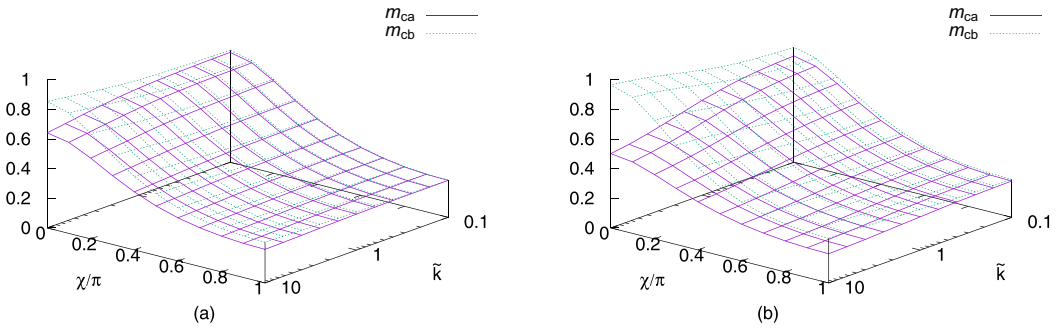

FIG. 2. Flow rate coefficients m_{Ca} and m_{Cb} [Eq. (A23)] as functions of $\tilde{k}$ and χ (BGKW model, $\varepsilon = 0.5$). (a) $c = 0.025$ and (b) $c = 0.1$. Solid line for m_{Ca} (inner rotation) and dotted line for m_{Cb} (outer rotation). These functions are symmetric with respect to $\chi = \pi$.

FIG. 3. Schematics of trajectories of collisionless molecules and the range of the direction of the molecular velocities arriving from the rotating cylinder. (a) Inner rotation and (b) outer rotation. The shaded area represents the directional range of molecular velocities arriving from the rotating cylinder. The thick arc in panel (b) indicates the directional range of the molecular velocities traveling from the outer cylinder to the outer cylinder, which is of $O(\sqrt{c})$.

We shall physically examine how the difference $m_{\rm Cb} - m_{\rm Ca}$ behaves as the Knudsen number increases. According to the Navier–Stokes solution (B37) in Appendix B, the difference $m_{\rm Cb} - m_{\rm Ca}$ is of $O(c)$, and it should remain so as long as $k \ll 1$. Now consider the opposite limit of large Knudsen number such that $ck^2 \gg 1$ so that the intermolecular collision is negligible. Figure 3 shows schematics of the trajectories of collisionless molecules arriving at a point in the gas from the rotating cylinder, and the shaded area represents the range of direction of these molecular velocities. Here, $ck^2 \gg 1$ means that intermolecular collisions are negligible even for the longest molecular path tangential to the inner cylinder [10,11]. Clearly, the range for the inner rotation [Fig. 3(a)] is narrower than that for the outer rotation [Fig. 3(b)]. The difference, indicated by the thick arc in Fig. 3(b), corresponds to the molecules traveling from the outer cylinder to the outer cylinder, which is proportional to $\sqrt{c}$ [11]. Molecules departing from the rotating cylinder will have larger circumferential momentum on average than those departing from the cylinder at rest. Thus, the circumferential momentum carried by the molecules for inner rotation will be smaller than that for outer rotation by an amount proportional to $\sqrt{c}$. For this reason, the difference $m_{\rm Cb} - m_{\rm Ca}$ in the flow rates increases from $O(c)$ to $O(\sqrt{c})$ with an increase in the Knudsen number. In fact, $m_{\rm Cb} - m_{\rm Ca} = O(\sqrt{c})$ for the infinite Knudsen number $\tilde{k} = \infty$, see Eq. (A33) in Appendix A. This feature is explicitly confirmed in Fig. 4, in which the difference $m_{\rm Cb} - m_{\rm Ca}$ at $\chi = 0$ is plotted as a function of c for various $\tilde{k}$ values. When $\tilde{k} = 0.1$ or 1, $c\tilde{k}^2$ remains small, and accordingly $m_{\rm Cb} - m_{\rm Ca}$ remains $O(c)$. However, when $\tilde{k} = 10$, $c\tilde{k}^2$ varies from 0.01 to 20. Accordingly, we can observe that the difference $m_{\rm Cb} - m_{\rm Ca}$ undergoes a transition from $O(c)$ to $O(\sqrt{c})$. In this discussion, eccentricity

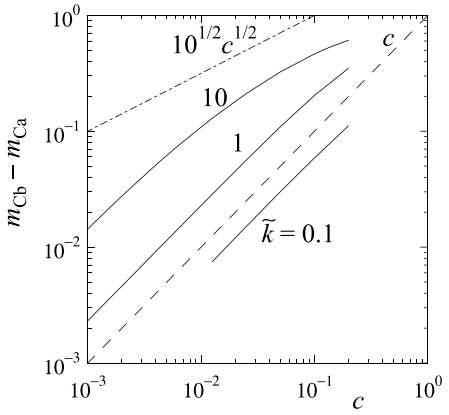

FIG. 4. The difference $m_{\rm Cb} - m_{\rm Ca}$ in the flow-rate coefficients of generalized Couette flows between outer and inner rotations as a function of the dimensionless curvature c for $\tilde{k} = 0.1$, 1, and 10 (BGKW model, $\varepsilon = 0.5$, $\chi = 0$). Dotted line represents c and dash-dotted line represents $10^{1/2}c^{1/2}$.

is inessential. Incidentally, the limit $\varepsilon \to 0$ (coaxial case) was discussed in Appendix C in Ref. [11]. According to it, the $\sqrt{c}$-dependence holds even in the coaxial case. However, the coaxial case yields a circumferentially uniform flow and thus no lubrication effect occurs, so this case is practically insignificant.

From Fig. 2, we can also observe that, as $\tilde{k}$ increases, m_{Cb} for the outer rotation increases, whereas m_{Ca} for the inner rotation decreases. This property can be understood as follows. From the linearity of the boundary-value problems Eqs. (A17) and (A18) and Eqs. (A19) and (A20) in Appendix A, the sum $\Phi_{\mathrm{Cb}} + \Phi_{\mathrm{Ca}}$ represents the solution of the flow in which both cylinders simultaneously rotate at the same unit circumferential velocity. The solution is nearly a rigid-body rotation because $c \ll 1$. Because the rigid-body rotation is the equilibrium solution of the Boltzmann equation for an arbitrary Knudsen number, we can expect

$$u_{\mathrm{Cb}} + u_{\mathrm{Ca}} = 1 + O(c) \tag{41}$$

for all $\tilde{k}$, where u_{Ca} and u_{Cb} are the normalized flow velocities appearing in Eq. (38). Equation (41) actually holds for the Navier–Stokes solution [Eq. (B38)] and for the free-molecular solution [Eq. (A32)]; it is also numerically confirmed for $0.1 \leqslant \tilde{k} \leqslant 10$. Accordingly, the sum $m_{\mathrm{Cb}} + m_{\mathrm{Ca}}$ of the flow rates (A23) is independent of $\tilde{k}$ neglecting the terms of $O(c)$. On the other hand, from Fig. 4, the difference $m_{\mathrm{Cb}} - m_{\mathrm{Ca}}$ increases from $O(c)$ to $O(\sqrt{c})$ as $\tilde{k}$ increases. Noting that $\sqrt{c} \gg c$, m_{Cb} must increase and m_{Ca} must decrease.

The properties of the flow-rate coefficients presented above play key roles in the remainder of this paper. A simple database of the functions m_{Ca} and m_{Cb} is provided in Appendix C, and the numerical data necessary for this database are available from Ref. [19].

D. Without curvature term model

Before closing this section, we briefly revisit the primitive analysis discussed in Sec. III A, i.e., treating the curvature term $c\zeta_\rho G \partial \hat{f}/\partial\theta_\zeta$ in Eq. (23) as a higher-order term. The analysis in this approach is quite similar to that in Sec. III B; the only difference is that the operator $\mathrm{D}'_{\mathrm{ec}}$ in Eq. (23) is replaced solely by the first term $(\gamma H)^{-1}\cos\theta_\zeta \partial/\partial y$. Further details of the analysis are given in Appendix D. Consequently, a lubrication equation is derived as

$$\frac{\mathrm{d}}{\mathrm{d}\chi}\left[m_{\mathrm{P}}^{\mathrm{woc}}\left(\frac{k}{\hat{p}_{(0)}}, \chi\right)\frac{\mathrm{d}\hat{p}_{(0)}}{\mathrm{d}\chi} + u_{wa}\hat{p}_{(0)} m_{\mathrm{Ca}}^{\mathrm{woc}}\left(\frac{k}{\hat{p}_{(0)}}, \chi\right) + u_{wb}\hat{p}_{(0)} m_{\mathrm{Cb}}^{\mathrm{woc}}\left(\frac{k}{\hat{p}_{(0)}}, \chi\right)\right] = 0, \tag{42}$$

which is of the same form as Eq. (37). The only difference is that the flow-rate coefficients m_{P}, m_{Ca}, and m_{Cb} in Eq. (37) are replaced by $m_{\mathrm{P}}^{\mathrm{woc}}$, $m_{\mathrm{Ca}}^{\mathrm{woc}}$, and $m_{\mathrm{Cb}}^{\mathrm{woc}}$ which are defined in Appendix D. Therefore, the difference in the solution arises only through these flow-rate coefficients. For brevity, Eq. (42) is referred to as the without curvature term (WOC) model.

The flow-rate coefficients exhibit the following prominent features. First, $m_{\mathrm{Ca}}^{\mathrm{woc}}$ and $m_{\mathrm{Cb}}^{\mathrm{woc}}$ are identical:

$$m_{\mathrm{Ca}}^{\mathrm{woc}} = m_{\mathrm{Cb}}^{\mathrm{woc}}. \tag{43}$$

Equation (43) is derived in Appendix D. This property arises because treating the curvature term as a higher-order term alters the characteristics of the Boltzmann equation (and so the trajectories shown in Fig. 3), and hence the numbers of molecules arriving from each cylinder are no longer distinguishable. Another feature of the WOC model is that $m_{\mathrm{Ca}}^{\mathrm{woc}}$ and $m_{\mathrm{Cb}}^{\mathrm{woc}}$ are independent of $\tilde{k}$, i.e.,

$$\frac{\partial m_{\mathrm{Ca}}^{\mathrm{woc}}}{\partial \tilde{k}} = \frac{\partial m_{\mathrm{Cb}}^{\mathrm{woc}}}{\partial \tilde{k}} = 0. \tag{44}$$

Equation (44) is also derived in Appendix D. The WOC model was discussed in Ref. [11] for the special case in which the $m_{\mathrm{Cb}}^{\mathrm{woc}}$ term was absent. Thus, the relations (43) and (44) are new findings of the present study. From the property (43), for example, we immediately find that the solution $\hat{p}_{(0)}$ of Eq. (42) for the inner rotation is identical with that for the outer rotation provided

that the circumferential velocity is the same. These properties are clearly inconsistent with those shown in Figs. 2 and 4 in Sec. III C. As a result, the WOC model (42) provides solutions that are inconsistent with those of Eq. (37). To establish which of them is correct, it is rational to compare the results with that of the direct numerical solution of the Boltzmann equation. To this end, a direct numerical analysis of the boundary-value problem (23)–(29) using a finite-difference method is conducted to provide the reference solution for the assessment. The numerical method used for this reference solution is presented in Sec. IV. The assessment against this reference solution is presented in Sec. V.

IV. DIRECT NUMERICAL ANALYSIS

A. Numerical method

This section describes the direct numerical analysis of the boundary-value problem (23)–(29). In the numerical analysis, we assume that the gas is governed by the BGKW kinetic equation. Specifically, the collision integral is given by

$$\hat{J}(\hat{f},\hat{f}) = \hat{\rho}(\hat{f}_e - \hat{f}),$$
$$\hat{f}_e = \frac{\hat{\rho}}{(\pi\hat{T})^{3/2}} \exp\left(-\frac{(\zeta_\rho\cos\theta_\zeta - \hat{v}_\eta)^2 + (\zeta_\rho\sin\theta_\zeta - \hat{v}_\chi)^2 + \zeta_z^2}{\hat{T}}\right), \tag{45}$$

where $\hat{\rho}$, $\hat{v}_\eta$, $\hat{v}_\chi$, and $\hat{T}$ are given by Eqs. (30a)–(30d). The mean free path ℓ of the BGKW model is related to the viscosity μ_0 of the gas according to [3]

$$\mu_0 = \gamma_1 \frac{\sqrt{\pi}}{2} \frac{p_0}{(2RT_0)^{1/2}} \ell, \tag{46}$$

where γ_1 is a constant determined by the molecular model, e.g., $\gamma_1 = 1$ for the BGKW model.

The method of numerical analysis is the same as that presented in Ref. [11], and it is thus outlined only briefly here. First, the following marginal distribution functions are introduced [20]:

$$g_f = \int_{-\infty}^{\infty} \hat{f}\,\mathrm{d}\zeta_z, \quad h_f = 2\int_{-\infty}^{\infty} \zeta_z^2 \hat{f}\,\mathrm{d}\zeta_z. \tag{47}$$

Multiplying both sides of Eqs. (23)–(28) by 1 or $2\zeta_z^2$ and integrating over $-\infty < \zeta_z < \infty$, we obtain a reduced boundary-value problem for g_f and h_f in the four-dimensional space y, χ, ζ_ρ, and θ_ζ, i.e., the fifth variable ζ_z is eliminated. Second, the semi-infinite range $0 \leqslant \zeta_\rho < \infty$ is replaced by the finite range $0 \leqslant \zeta_\rho \leqslant \zeta_D$, where ζ_D is a constant such that the distribution functions g_f and h_f are sufficiently small around $\zeta_\rho = \zeta_D$. Third, rectangular mesh points are arranged in the finite four-dimensional domain $0 \leqslant y \leqslant 1$, $0 \leqslant \chi \leqslant 2\pi$, $0 \leqslant \zeta_\rho \leqslant \zeta_D$, and $-\pi \leqslant \theta_\zeta \leqslant \pi$. The boundary-value problem (23)–(29) is then discretized and solved numerically using a finite-difference method.

Because the inner cylinder is convex, the distribution function $\hat{f}$ of the gas is discontinuous [3] across a surface in the three-dimensional phase space of y, θ_ζ, and χ. So we employ the hybrid scheme combining characteristic coordinate and finite difference methods devised in Ref. [21]. One of the features of the present problem is that the BGKW equation is written in a bipolar coordinate system. Owing to this, the numerical analysis is considerably more complicated than that in Refs. [10] and [21]. Details of the numerical analysis, along with difficulties arising from the bipolar coordinates and their remedies, are provided in Ref. [11].

B. Computational conditions and accuracy tests

The computational conditions are as follows. For the y coordinate, $N_y + 1$ mesh points are arranged nonuniformly in the interval $0 \leqslant y \leqslant 1$, where $N_y = 100$. The minimum mesh size is

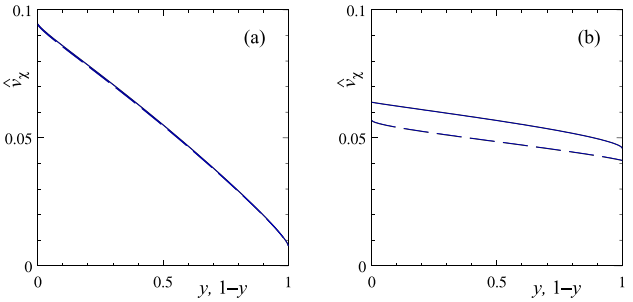

FIG. 5. Profile of the dimensionless flow velocity $\hat{v}_\chi$ at the cross section $\chi = \pi$ ($c = 0.025$, $\varepsilon = 0.5$). (a) $k = 0.1$ and (b) $k = 10$. Solid lines (—) for the outer rotation $\hat{v}_{wa} = 0$, $\hat{v}_{wb} = 0.1$; dashed lines (– –) for the inner rotation $\hat{v}_{wa} = 0.1$, $\hat{v}_{wb} = 0$. $\hat{v}_\chi$ is plotted as a function of y for the inner rotation whereas plotted as a function of $1 - y$ for the outer rotation. Thin blue lines for the direct numerical solution and thick black lines for the solution of the lubrication model (37) and (38). Blue and black lines are indistinguishable.

0.0021 at $y = 0$ and $y = 1$, and the maximum size is 0.0125 on the interval $0.1 \leqslant y \leqslant 0.9$. For χ, $N_x + 1$ mesh points are arranged uniformly in the interval $0 \leqslant \chi \leqslant 2\pi$, where $N_x = 200$. For ζ_ρ, $N_u + 1$ mesh points are arranged uniformly in the interval $0 \leqslant \zeta_\rho \leqslant \zeta_D$, where $N_u = 40$ and $\zeta_D = 5$. For θ_ζ, $N_v + 1$ mesh points are arranged uniformly in the interval $-\pi \leqslant \theta_\zeta \leqslant \pi$, where $N_v = 400$.

The results of accuracy tests are as follows:

(1) Conservation law. According to Eq. (31), the dimensionless mass-flow rate $\int_0^1 H\hat{\rho}\hat{v}_\chi \mathrm{d}y$ is theoretically independent of χ. Thus, the uniformity of this quantity serves as a measure of the accuracy. The variation in the mass-flow rate using the present computational scheme over $0 \leqslant \chi \leqslant 2\pi$ is less than 1.8% when $\hat{v}_{wa} = 0$, $\hat{v}_{wb} = 0.1$, or less than 14% when $\hat{v}_{wa} = -0.1$, $\hat{v}_{wb} = 0.1$. In the latter case, due to the opposing rotation $\hat{v}_{wa} = -\hat{v}_{wb}$, the net mass flow rate is so small that even very small error is magnified.

(2) Dependence on the mesh system. To test the accuracy, in addition to the production run P with $(N_y, N_x, N_u, N_v) = (100, 200, 40, 400)$, we conducted recomputations using a coarser mesh system A with $(N_y, N_x, N_u, N_v) = (50, 100, 32, 200)$, and the coarsest system B with $(N_y, N_x, N_u, N_v) = (24, 50, 32, 100)$. First, by examining the differences among the three runs, i.e., P–A and P–B for a few samples, the convergence speed is estimated. Then, the error in the production run P is estimated from the difference P–A. From this test, it is estimated that the numerical error in the dimensionless normal stress $\hat{p}_{\eta\eta}$ over $0 \leqslant \chi \leqslant 2\pi$ at $y = 0$ is less than 0.18% when $\hat{v}_{wa} = 0$, $\hat{v}_{wb} = 0.1$, or less than 0.42% when $-\hat{v}_{wa} = \hat{v}_{wb} = 0.1$, and that the numerical error in the flow velocity $\hat{v}_\chi$ over $0 \leqslant y \leqslant 1$ at the cross-section $\chi = 0$ is less than 0.05% when $\hat{v}_{wa} = 0$, $\hat{v}_{wb} = 0.1$, or less than 0.28% when $-\hat{v}_{wa} = \hat{v}_{wb} = 0.1$. Furthermore, the numerical error in the magnitude $(F_1^2 + F_2^2)^{1/2}$ of the eccentric force (18) is estimated to be less than 0.21% when $\hat{v}_{wa} = 0$, $\hat{v}_{wb} = 0.1$, or less than 1.4% when $-\hat{v}_{wa} = \hat{v}_{wb} = 0.1$.

V. RESULTS AND DISCUSSION

A. Outer rotation vs inner rotation

We first examine the difference between the two flows of the outer and inner rotations, i.e., one flow in which only the outer cylinder rotates, and the other in which only the inner cylinder rotates at the same circumferential velocity. The dimensionless flow velocity $\hat{v}_\chi$ at the cross section $\chi = \pi$ is presented in Fig. 5. The goal of this presentation is to verify the discussion regarding the circumferential momentum of the gas induced by the motion of the boundary in Fig. 3. We choose the cross section $\chi = \pi$ because the pressure gradient, which is another source of the flow, is small there, see the next paragraph. The solid lines represent the results for outer rotation, and the dashed

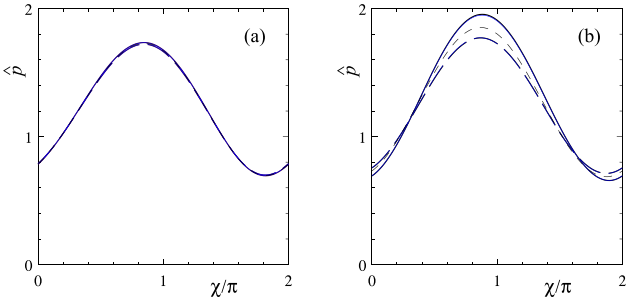

FIG. 6. Distribution of the dimensionless pressure $\hat{p}$ on the inner cylinder I: outer rotation vs inner rotation ($c = 0.025$, $\varepsilon = 0.5$, $y = 0$). (a) $k = 0.1$ and (b) $k = 10$. See the caption of Fig. 5 for the meaning of the lines. Thin dotted line (- - -) for the solution of Eq. (42), for which results for outer and inner rotations coincide.

lines represent those for inner rotation. For the outer rotation, $\hat{v}_\chi$ is plotted as a function of $1 - y$ (a mirror image with respect to $y = 1/2$), because a direct comparison would be less meaningful due to the difference in the moving boundary. The thin blue lines represent the direct numerical solution of the boundary-value problem (23)–(29), which is the reference solution, and the thick black lines represent the solution of the lubrication model (37) and (38). The results of inner rotation for $c = 0.025$ are newly computed in this paper. When the Knudsen number is small [Fig. 5(a)], the results for the inner and outer rotations are almost indistinguishable. When the Knudsen number is large [Fig. 5(b)], in contrast, considerable difference is observed. The outer rotation (solid line) yields a larger flow velocity, i.e., a larger circumferential momentum in the gas. Note that the difference in the bulk gas is approximately 20%, and this is of the order of $\sqrt{c}$ ($= 0.158$) much larger than c ($= 0.025$). These results support the discussion regarding Fig. 3 in Sec. III C. The solutions of the lubrication model (37) and (38) are in excellent agreement with the reference solution for both small and large Knudsen numbers.

The pressure distribution along the channel is presented in Fig. 6 as a function of the longitudinal coordinate χ. The meanings of the lines in the figure are the same as those in Fig. 5. The dotted line represents the solution of the WOC model (42), for which the results for the outer and inner rotations coincide. We begin by examining the results on the basis of the direct numerical solution (thin blue lines). The pressure rises over the interval $0 < \chi < \pi$ because the flow is converging there, and so the maximum of the pressure is attained at slightly ahead of $\chi = \pi$. When the Knudsen number is small [Fig. 6(a)], the pressure distributions of the two flows are almost indistinguishable. When the Knudsen number is large [Fig. 6(b)], however, considerable difference is observed. The outer rotation (solid line) yields the greater pressure variation. This behavior can be easily understood by considering the lubrication Eq. (37). According to Eq. (37), the source of the pressure gradient $d\hat{p}_{(0)}/d\chi$ is the second and third terms in the square brackets, which represent the wedge action, i.e., the effect of the surface motion pushing the gas into the converging channel. The second term is absent for the outer rotation ($\hat{v}_{wa} = 0$) and the third term is absent for the inner rotation ($\hat{v}_{wb} = 0$). As we saw in Fig. 2, the coefficient m_{Cb} is significantly greater than m_{Ca} when $\tilde{k}$ is large, leading to a greater pressure gradient for the outer rotation. In this explanation, we implicitly assumed that the variation of the pressure $\hat{p}$ from unity is not so large; note that the coefficients m_{Ca}, etc., are influenced by the pressure variation through the first argument $k/\hat{p}_{(0)}$. This remark is omitted in the following discussion. We now compare the solutions of the lubrication Eqs. (37) and (42) with the reference solution. The solution of Eq. (37) agrees perfectly with the reference solution for both small and large Knudsen numbers. The solution of (42) agrees well when $k = 0.1$, but it does not when $k = 10$. As noted in Sec. III D, Eq. (42) yields identical solutions for the inner and outer rotations. This claim clearly contradicts the reference solution.

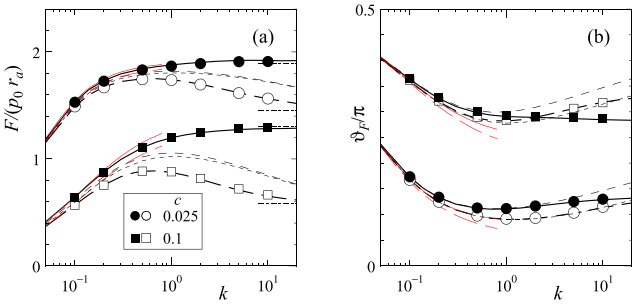

FIG. 7. Eccentric force (18) acting on the inner cylinder as a function of the Knudsen number I: outer rotation vs inner rotation ($\varepsilon = 0.5$). (a) Magnitude F and (b) the direction ϑ_F [Eq. (48)]. Closed symbols and the solid lines for the outer rotation $\hat{v}_{wa} = 0$, $\hat{v}_{wb} = 0.1$; open symbols and the dashed lines for the inner rotation $\hat{v}_{wa} = 0.1$, $\hat{v}_{wb} = 0$. Symbols for the direct numerical solution; thick black lines for the solution of Eqs. (37) and (40); thin red lines for the Navier–Stokes solution with slip [Eqs. (B25) and (B28)]. Thin dotted and fine dotted lines, respectively, for the outer and inner rotation solutions of the WOC model (42) and (D8). The dash-dotted lines in panel (a) are asymptotes of the direct numerical solutions as $k \to \infty$.

We now examine the eccentric force acting on the inner cylinder. Let the magnitude F and the direction ϑ_F of the eccentric force (18) be defined by

$$F_1 = F \cos \vartheta_F, \quad F_2 = -F \sin \vartheta_F. \tag{48}$$

The directions $\vartheta_F = 0$ and $\vartheta_F = \pi/2$ correspond, respectively, to X_1 and $-X_2$ directions in Fig. 1(a). The magnitude F and the direction ϑ_F are presented in Figs. 7(a) and 7(b), respectively. The closed symbols and solid lines represent the results for the outer rotation, and the open symbols and dashed lines represent those for the inner rotation. Symbols represent the direct numerical (reference) solution, and the thick lines represent the solution of the lubrication model (37) and (40). The thin dotted and fine dotted lines represent the solutions of the WOC model (42) and (D8) for the outer and inner rotations, respectively. We focus on the magnitude F [Fig. 7(a)]. The results for the outer and inner rotations are very close for small Knudsen numbers, but the difference becomes evident as the Knudsen number increases, as expected from Fig. 6. The outer rotation yields the greater eccentric force. For the inner rotation (open symbols), the magnitude F reaches the maximum at approximately $k = 1$, and it decreases with a further increase in k. In contrast, for the outer rotation (closed symbols), the increase or decrease in the magnitude F is more delicate. This Knudsen-number dependence of the eccentric force can also be explained by the lubrication Eq. (37). According to Eq. (37), the pressure gradient $\mathrm{d}\hat{p}_{(0)}/\mathrm{d}\chi$ is, roughly speaking, determined by the relative magnitudes of the two factors: the coefficient $m_{\mathrm{P}}(< 0)$ multiplied by $\mathrm{d}\hat{p}_{(0)}/\mathrm{d}\chi$ and the sum of the second and third terms (wedge-action terms). First, consider the inner rotation, in which only the u_{wa} term of the wedge action is present. The coefficient $-m_{\mathrm{P}}$ of the generalized Poiseuille flow reaches the minimum (Knudsen minimum) at approximately $\tilde{k} = 1$ and increases with $\tilde{k}$ thereafter [11]. The coefficient m_{Ca} decreases monotonically with an increase in $\tilde{k}$ as shown in Fig. 2. Therefore, the pressure gradient and thus the eccentric force must decrease with an increase in the Knudsen number beyond unity. Second, consider the outer rotation, in which the u_{wb} term is present in Eq. (37). In this case, both m_{Cb} and $-m_{\mathrm{P}}$ increase with $\tilde{k}$, so the dependence of the pressure gradient and thus the eccentric force on the Knudsen number is more delicate and is determined by the relative rate of growth of the two factors. According to the reference solution, F is nearly constant for a large k. F for $k = \infty$ is slightly greater than that at $k = 10$ when $c = 0.1$, whereas slightly smaller when $c = 0.025$.

Let us examine the performance of the lubrication model (37) and (40) and the WOC model (42) and (D8). The results of the former (thick solid and dashed lines) agree perfectly with the reference

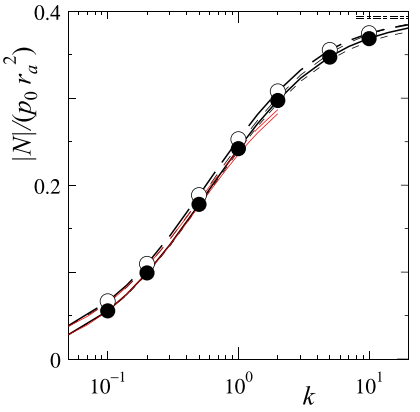

FIG. 8. Torque (19) acting on the inner cylinder as a function of the Knudsen number I: outer rotation vs inner rotation ($c = 0.025$, $\varepsilon = 0.5$). See the caption of Fig. 7. The dash-dotted lines are asymptotes of the direct numerical solutions as $k \to \infty$, where the results for inner and outer rotation are almost indistinguishable.

solution over the entire range of the Knudsen number. The solution of the WOC model (thin dotted and fine dotted lines) does not agree with the reference solution except at small Knudsen numbers. Moreover, the difference between the outer and inner rotations is too small, which is a consequence of the coincidence in the pressure (Fig. 6). Therefore, both Figs. 6 and 7 provide clear examples that the WOC model does not work even qualitatively at large Knudsen numbers.

Finally, the torque N [Eq. (19)] acting on the inner cylinder is presented in Fig. 8. The torque depends on the dimensionless curvature c only slightly [11], so only the case of $c = 0.025$ is presented. The torque is a monotonically increasing function of the Knudsen number k. The result for the outer rotation is close to that of the inner rotation over the whole range of k. In contrast to Fig. 7, the difference between outer and inner rotations does not increase with an increase in k. This may be understood as follows. The torque (19) is determined by the shear stress $\hat{p}_{\chi\eta}$. According to the analysis in Sec. III, the shear stress (40) is composed of the two parts: one that is proportional to the pressure gradient $\mathrm{d}\hat{p}_{(0)}/\mathrm{d}\chi$ and the other proportional to the rotation speeds of the cylinders. The numerical solution of Eq. (40) shows that the contribution of the former is small compared with the latter. Thus, the difference in the pressure gradient appeared in Fig. 6 does not affect the shear stress much. The solution of Eq. (40) agrees with the reference solution very well.

B. Simultaneous rotation of the cylinders in opposite directions

Next, we study a flow in which the two cylinders rotate simultaneously at the same circumferential speed but in opposite directions, i.e., $\hat{v}_{wa} = -\hat{v}_{wb}$. Note that this flow is not a superposition of the two flows in Sec. V A; it is a nonlinear problem due to a finite pressure variation. The pressure distribution is presented in Fig. 9 as a function of χ. When the Knudsen number is small [Fig. 9(a)], the pressure variation is very small. This result is expected because the flow-rate coefficients are so close [$m_{\mathrm{Cb}} - m_{\mathrm{Ca}} = O(c)$] that the wedge action, i.e., the second and third terms in the square brackets in Eq. (37), almost cancels out. When the Knudsen number is large [Fig. 9(b)], considerable pressure variation occurs. This nonsmall pressure variation arises because the cancellation of $m_{\mathrm{Cb}} - m_{\mathrm{Ca}}$ no longer occurs for a large Knudsen number, as shown in Fig. 2. The solution of Eq. (37) agrees well with the reference solution for a large Knudsen number, but a nonnegligible disagreement is observed for a small Knudsen number [Fig. 9(a)]. This disagreement appears because the variation in the pressure is so small that the numerical error in the reference solution is no longer negligible; note that Fig. 9(a) is vertically magnified from Fig. 9(b). The

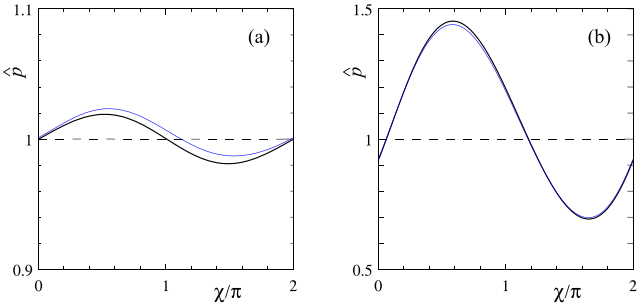

FIG. 9. Distribution of the dimensionless pressure $\hat{p}$ on the inner cylinder II: simultaneous rotation in opposite directions ($c = 0.025$, $\varepsilon = 0.5$, $-\hat{v}_{wa} = \hat{v}_{wb} = 0.1$, $y = 0$). (a) $k = 0.1$ and (b) $k = 10$. Thin blue lines for the direct numerical solution; thick black lines for the solution of Eq. (37). Dotted line for the solution of Eq. (42), for which $\hat{p} = \text{const} = 1$.

pressure gradient of WOC model (42) vanishes identically due to Eq. (43), irrespective of the Knudsen number.

The eccentric force acting on the inner cylinder is presented in Fig. 10 as a function of the Knudsen number k. As expected from Fig. 9, the magnitude F is small for a small k, but it grows considerably as k increases. A key feature in Fig. 10(a) is that F is almost independent of the dimensionless curvature c when $k \ll 1$, whereas it increases with a decrease in c when $k \gg 1$. To analyze this c dependence of the solution, we write the lubrication equation (37) in terms of $\hat{v}_{wb}$ to avoid using $u_{wb} (= \hat{v}_{wb}/c)$:

$$\frac{\mathrm{d}}{\mathrm{d}\chi}\left(m_{\mathrm{P}}\frac{\mathrm{d}\hat{p}_{(0)}}{\mathrm{d}\chi} + \hat{v}_{wb}\hat{p}_{(0)}\frac{m_{\mathrm{Cb}} - m_{\mathrm{Ca}}}{c}\right) = 0. \tag{49}$$

When k so is small that $ck^2 \ll 1$, $m_{\mathrm{Cb}} - m_{\mathrm{Ca}} = O(c)$, as seen in Fig. 4. Thus, the second term in the parentheses in Eq. (49) is almost independent of c, so also is the eccentric force. (Note that m_{P} depends on c only weakly [11].) In contrast, when k is so large that $ck^2 \gg 1$, $m_{\mathrm{Cb}} - m_{\mathrm{Ca}} = O(\sqrt{c})$, meaning that the second term in the parentheses is of $O(1/\sqrt{c})$, and it thus increases with a decrease in c keeping $\hat{v}_{wb}$ constant, to raise the pressure gradient. In Fig. 10(b), the direction ϑ_F of the eccentric force is close to $\pi/2$ when k is small. When k is small, as we saw in Fig. 9(a), the pressure

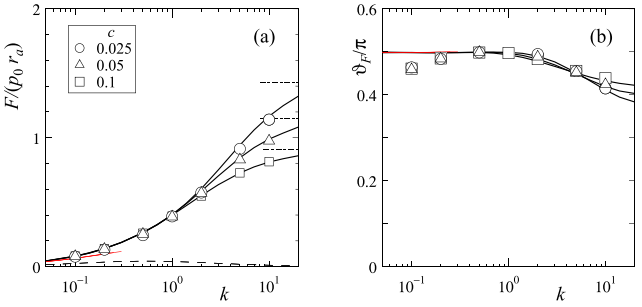

FIG. 10. Eccentric force (18) acting on the inner cylinder as a function of the Knudsen number II: simultaneous rotation in opposite directions ($\varepsilon = 0.5$, $-\hat{v}_{wa} = \hat{v}_{wb} = 0.1$). (a) Magnitude F and (b) the direction ϑ_F [Eq. (48)]. Symbols for the direct numerical solution; thick black lines for the solution of Eqs. (37) and (40); thin red lines for the Navier–Stokes solution with slip [Eqs. (B25) and (B28)]. Thin dotted line in panel (a) for the solutions of Eqs. (42) and (D8), whose dependence on c is almost indistinguishable. The dash-dotted lines in panel (a) are asymptotes of the direct numerical solutions as $k \to \infty$; from the top, $c = 0.025$, 0.05, and 0.1.

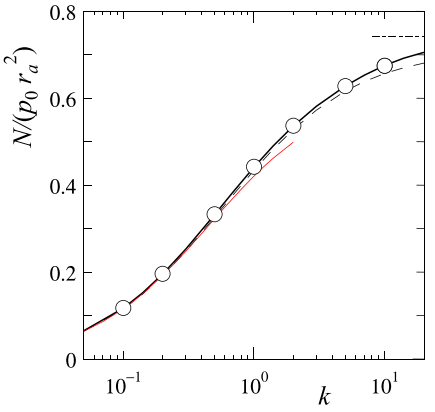

FIG. 11. Torque (19) acting on the inner cylinder as a function of the Knudsen number II: simultaneous rotation in opposite directions ($c = 0.025$, $\varepsilon = 0.5$, $-\hat{v}_{wa} = \hat{v}_{wb} = 0.1$). See the caption of Fig. 10.

variation is so small that the flow problem may be linearized. In the linearized system, we can show [22] that the pressure $\hat{p} - 1$ is antisymmetric [see Fig. 9(a)] and the shear stress $\hat{p}_{\chi\eta}$ is symmetric with respect to $\chi = \pi$ under the present symmetric configuration $h(\eta, \chi) = h(\eta, 2\pi - \chi)$ of the channel. Consequently, from Eq. (18), F_1 vanishes to yield $\vartheta_F = \pi/2$.

The performance of the lubrication model (37) and (40) and the WOC model (42) and (D8) is now examined. As for the magnitude F in Fig. 10(a), the solution of the former (solid line) agrees very well with the reference solution over the entire range of the Knudsen number k. As for the direction ϑ_F in Fig. 10(b), however, a nonnegligible disagreement is observed around $k = 0.1$. In view of the agreement with the Navier–Stokes solution (thin red line), the solution of Eqs. (37) and (40) should be correct. This disagreement is attributed to the inevitable numerical errors in the direct numerical solution. When $k \ll 1$, as shown in Fig. 10(a), the eccentric force is close to zero. Therefore, even a very small error in F_1 or F_2 can lead to a nonnegligible error in ϑ_F due to the relation $\tan \vartheta_F = -F_2/F_1 \simeq 0/0$. In other words, the solution of the lubrication model (37) and (40) serves to compensate for the direct numerical solution when the latter is difficult to conduct. The WOC model (dotted line) yields $F = O(c)$ regardless of k. This occurs because the pressure gradient $\mathrm{d}\hat{p}_{(0)}/\mathrm{d}\chi$ vanishes identically (see Fig. 9), and thus only the terms multiplied by u_{wa} and u_{wb} in the shear stress (D8) contribute to the eccentric force. Therefore, the WOC model is absolutely of no use for studying the present flow. We emphasize that all the poor performance of the WOC model presented in this section arises from the only one procedure in the slowly varying analysis that the apparently small curvature term $c\zeta_\rho G \partial \hat{f}/\partial\theta_\zeta$ in the Boltzmann equation is treated as a higher-order term.

Finally, the torque N acting on the inner cylinder is presented in Fig. 11, where $N > 0$. The magnitude of the torque is approximately twice of that in Fig. 8, because the opposing rotation strengthens rather reduces the torque. The overall characteristic is similar to that in Fig. 8. The result of Eq. (40) agrees with the reference solution very well.

Before closing this section, we discuss the relation of the present study to our previous study [14], in which the effect of heating the cylinders on the eccentric force in the same setting as Fig. 1 (but $v_{wb} = 0$) was discussed. One of the important findings was that the impact of heating either of the cylinders is small at small Knudsen numbers, but becomes significant as the Knudsen number increases. Specifically, heating the inner cylinder reduces the eccentric force, whereas heating the outer cylinder enhances it. The mechanism behind this phenomenon is somewhat similar to that elucidated in the present study. That is, the transfer of circumferential momentum carried by collisionless molecules from the rotating inner cylinder decreases with heating the inner cylinder and increases with heating the outer cylinder. However, there is a crucial difference from the present

study. In Ref. [14], this reduction or enhancement was caused by a decrease or increase in the density of the gas near the rotating cylinder due to heating, and the curvature was not a significant factor. In the present study, as emphasized, the curvature is decisively essential.

VI. CONCLUSION

In this paper, we studied a microscale lubrication flow of a gas between eccentric circular cylinders on the basis of kinetic theory. This study extends the work reported in Ref. [11] by allowing for rotation of the outer cylinder. The dimensionless curvature c was small and the Knudsen number was arbitrary. The Boltzmann equation was studied analytically using an improved slowly varying approximation. A generalized lubrication equation, which is an extension of that in Ref. [11], was derived. To assess the accuracy of this equation, a direct numerical analysis of the BGKW model of the Boltzmann equation was also conducted to provide the reference solution. The main conclusions are as follows.

(i) Comparison of outer and inner rotation flows at the same circumferential velocity. When the Knudsen number is small, there is almost no difference between the two flows. However, as the Knudsen number increases, significant differences emerge. The outer rotation yields a greater eccentric force acting on the inner cylinder.

(ii) Simultaneous rotation of the cylinders in opposite directions. When the Knudsen number is small, the eccentric force almost vanishes due to the cancellation of the wedge action as a consequence of the opposing rotations. As the Knudsen number increases, this cancellation diminishes, leading to a finite eccentric force. For small Knudsen numbers, the eccentric force is almost independent of the dimensionless curvature c, whereas it increases with a decrease in c for large Knudsen numbers. These phenomena, as well as that in the first item above, are caused by the fact that the difference between the two flow-rate coefficients of Couette flows for the outer and inner rotations in the slowly varying solution undergoes a transition from $O(c)$ to $O(\sqrt{c})$ as the Knudsen number increases. This is genuinely a noncontinuum effect due to the curvature of the surfaces.

(iii) The solution of the generalized lubrication equation agrees excellently with the reference solution over the whole range of the Knudsen number. In contrast, the WOC model produces solutions that qualitatively contradict the reference solution when the Knudsen number is large. This poor performance of the WOC model originates from the only procedure in the slowly varying analysis that the small curvature term in the Boltzmann equation was treated as a higher order term.

ACKNOWLEDGMENT

This work was supported by JSPS KAKENHI Grant No. 24K07324.
The author declares no conflict of interest.

DATA AVAILABILITY

The data for Appendix C are available in Ref. [19]. Other data that support the findings of this study are available from the corresponding author upon reasonable request.

APPENDIX A: DETAILS OF THE ANALYSIS

The boundary-value problem that governs the leading-order solution $\hat{f}_{(0)}$ is given by

$$\zeta_\rho \mathrm{D}'_{\mathrm{ec}} \hat{f}_{(0)} = \frac{1}{k} \hat{J}(\hat{f}_{(0)}, \hat{f}_{(0)}), \tag{A1}$$

$$\hat{f}_{(0)} = \hat{\sigma}_{a(0)} E \quad (y = 0,\ \cos\theta_\zeta > 0), \tag{A2}$$

$$\hat{f}_{(0)} = \hat{\sigma}_{b(0)} E \quad (y = 1,\ \cos\theta_\zeta < 0), \tag{A3}$$

$$\hat{\sigma}_{a(0)} = -2\sqrt{\pi}\iiint_{\cos\theta_\zeta<0} \zeta_\rho^2 \cos\theta_\zeta \hat{f}_{(0)} \mathrm{d}\zeta_\rho \mathrm{d}\theta_\zeta \mathrm{d}\zeta_z \quad (y=0),$$

$$\hat{\sigma}_{b(0)} = 2\sqrt{\pi}\iiint_{\cos\theta_\zeta>0} \zeta_\rho^2 \cos\theta_\zeta \hat{f}_{(0)} \mathrm{d}\zeta_\rho \mathrm{d}\theta_\zeta \mathrm{d}\zeta_z \quad (y=1),$$

$$\int_0^{2\pi} \mathrm{d}\chi \int_0^1 \mathrm{d}y H^2 \iiint \zeta_\rho \hat{f}_{(0)} \mathrm{d}\zeta_\rho \mathrm{d}\theta_\zeta \mathrm{d}\zeta_z = \frac{2\pi}{\gamma}. \tag{A4}$$

A solution is an equilibrium state at rest:

$$\hat{f}_{(0)} = C_{(0)} E, \tag{A5}$$

where $C_{(0)}$ can be an arbitrary function of χ as long as (A4) is satisfied. Here, $C_{(0)}$ is identified with the leading term $\hat{p}_{(0)}$ of the expansion $\hat{p} = \hat{p}_{(0)} + \hat{p}_{(1)} c + \cdots$ of the pressure $\hat{p}$, so we hereafter write $\hat{p}_{(0)}$ for $C_{(0)}$. Similarly, $\hat{\sigma}_{a(0)} = \hat{\sigma}_{b(0)} = C_{(0)} = \hat{p}_{(0)}$.

The boundary-value problem for the first-order solution $\hat{f}_{(1)}$ is a linear and inhomogeneous one given by

$$\zeta_\rho \mathrm{D}'_{\mathrm{ec}} \hat{f}_{(1)} = \frac{2}{k} \hat{J}(\hat{f}_{(0)}, \hat{f}_{(1)}) - \frac{\zeta_\rho \sin\theta_\zeta}{H} \frac{\partial \hat{f}_{(0)}}{\partial \chi}, \tag{A6}$$

$$\hat{f}_{(1)} = (\hat{\sigma}_{a(1)} + 2u_{wa} \hat{p}_{(0)} \zeta_\rho \sin\theta_\zeta) E \quad (y=0,\ \cos\theta_\zeta > 0), \tag{A7}$$

$$\hat{f}_{(1)} = (\hat{\sigma}_{b(1)} + 2u_{wb} \hat{p}_{(0)} \zeta_\rho \sin\theta_\zeta) E \quad (y=1,\ \cos\theta_\zeta < 0), \tag{A8}$$

$$\hat{\sigma}_{a(1)} = -2\sqrt{\pi}\iiint_{\cos\theta_\zeta<0} \zeta_\rho^2 \cos\theta_\zeta \hat{f}_{(1)} \mathrm{d}\zeta_\rho \mathrm{d}\theta_\zeta \mathrm{d}\zeta_z \quad (y=0),$$

$$\hat{\sigma}_{b(1)} = 2\sqrt{\pi}\iiint_{\cos\theta_\zeta>0} \zeta_\rho^2 \cos\theta_\zeta \hat{f}_{(1)} \mathrm{d}\zeta_\rho \mathrm{d}\theta_\zeta \mathrm{d}\zeta_z \quad (y=1),$$

$$\int_0^{2\pi} \mathrm{d}\chi \int_0^1 \mathrm{d}y H^2 \iiint \zeta_\rho \hat{f}_{(1)} \mathrm{d}\zeta_\rho \mathrm{d}\theta_\zeta \mathrm{d}\zeta_z = \frac{\pi}{\gamma}. \tag{A9}$$

The curvature term $\zeta_\rho \sin\chi \cos\theta_\zeta (\sinh\eta_a)^{-1} \partial \hat{f}_{(0)} / \partial\theta_\zeta$, which ought to appear as an inhomogeneous term, vanishes because the leading-order solution (A5) is independent of θ_ζ. The solution $\hat{f}_{(1)}$ is sought as a sum $\hat{f}_{(1)} = \hat{f}_{(1)}^{\mathrm{even}} + \hat{f}_{(1)}^{\mathrm{odd}}$ of even ($\hat{f}_{(1)}^{\mathrm{even}}$) and odd ($\hat{f}_{(1)}^{\mathrm{odd}}$) functions with respect to θ_ζ. Because the operator $\mathrm{D}'_{\mathrm{ec}}$ preserves the parity in θ_ζ, the problem is decomposed into separate sets of the boundary-value problems for $\hat{f}_{(1)}^{\mathrm{even}}$ and $\hat{f}_{(1)}^{\mathrm{odd}}$. A solution of the former is a Maxwellian at rest [11]:

$$\hat{f}_{(1)}^{\mathrm{even}} = C_{(1)} E, \tag{A10}$$

where $C_{(1)}$ is an arbitrary function of χ subject to Eq. (A9).

The odd function $\hat{f}_{(1)}^{\mathrm{odd}}$ can be reduced to a simpler problem by putting $\hat{f}_{(1)}^{\mathrm{odd}} = \hat{f}_{(0)} \phi$, to yield

$$\zeta_\rho \mathrm{D}'_{\mathrm{ec}} \phi = \frac{\hat{p}_{(0)}}{k} \mathcal{L}(\phi) - \frac{\zeta_\rho \sin\theta_\zeta}{H} \frac{1}{\hat{p}_{(0)}} \frac{\mathrm{d}\hat{p}_{(0)}}{\mathrm{d}\chi}, \tag{A11}$$

$$\phi = 2u_{wa} \zeta_\rho \sin\theta_\zeta \quad (y=0, \cos\theta_\zeta > 0), \tag{A12}$$

$$\phi = 2u_{wb} \zeta_\rho \sin\theta_\zeta \quad (y=1, \cos\theta_\zeta < 0), \tag{A13}$$

where $\mathcal{L}(\cdot)$ is the linearized collision operator defined by $E\mathcal{L}(\phi) = 2\hat{J}(E, E\phi)$. Because of the linearity, the solution is given by

$$\phi(y, \chi, \boldsymbol{\zeta}) = \frac{1}{\hat{p}_{(0)}} \frac{\mathrm{d}\hat{p}_{(0)}}{\mathrm{d}\chi} \Phi_{\mathrm{P}}\left(y, \boldsymbol{\zeta}; \frac{k}{\hat{p}_{(0)}}, \chi\right) + u_{wa}\Phi_{\mathrm{Ca}}\left(y, \boldsymbol{\zeta}; \frac{k}{\hat{p}_{(0)}}, \chi\right) + u_{wb}\Phi_{\mathrm{Cb}}\left(y, \boldsymbol{\zeta}; \frac{k}{\hat{p}_{(0)}}, \chi\right), \tag{A14}$$

where $\boldsymbol{\zeta}$ is an abbreviation for $(\zeta_\rho, \theta_\zeta, \zeta_z)$. The functions $\Phi_{\mathrm{P}}(y, \boldsymbol{\zeta}; \tilde{k}, \chi)$, $\Phi_{\mathrm{Ca}}(y, \boldsymbol{\zeta}; \tilde{k}, \chi)$, and $\Phi_{\mathrm{Cb}}(y, \boldsymbol{\zeta}; \tilde{k}, \chi)$ are the solutions of the following boundary-value problems: for Φ_{P} (generalized Poiseuille flow),

$$\zeta_\rho \mathrm{D}'_{\mathrm{ec}}\Phi_{\mathrm{P}} - \frac{1}{\tilde{k}}\mathcal{L}(\Phi_{\mathrm{P}}) = -\frac{\zeta_\rho \sin\theta_\zeta}{H}, \tag{A15}$$

$$\Phi_{\mathrm{P}} = 0 \quad (y = 0,\ \cos\theta_\zeta > 0 \text{ and } y = 1,\ \cos\theta_\zeta < 0), \tag{A16}$$

for Φ_{Ca} (Couette flow for inner rotation),

$$\zeta_\rho \mathrm{D}'_{\mathrm{ec}}\Phi_{\mathrm{Ca}} - \frac{1}{\tilde{k}}\mathcal{L}(\Phi_{\mathrm{Ca}}) = 0, \tag{A17}$$

$$\Phi_{\mathrm{Ca}} = 2\zeta_\rho \sin\theta_\zeta \ \ (y = 0,\ \cos\theta_\zeta > 0), \quad \Phi_{\mathrm{Ca}} = 0 \ \ (y = 1,\ \cos\theta_\zeta < 0), \tag{A18}$$

and for Φ_{Cb} (Couette flow for outer rotation),

$$\zeta_\rho \mathrm{D}'_{\mathrm{ec}}\Phi_{\mathrm{Cb}} - \frac{1}{\tilde{k}}\mathcal{L}(\Phi_{\mathrm{Cb}}) = 0, \tag{A19}$$

$$\Phi_{\mathrm{Cb}} = 0 \ \ (y = 0,\ \cos\theta_\zeta > 0), \quad \Phi_{\mathrm{Cb}} = 2\zeta_\rho \sin\theta_\zeta \ \ (y = 1,\ \cos\theta_\zeta < 0). \tag{A20}$$

Note that the solution of Eqs. (A19) and (A20) is not simply the mirror image of that of Eqs. (A17) and (A18) with respect to $y = 1/2$ because the operator $\mathrm{D}'_{\mathrm{ec}}$ depends on y explicitly through $H(y, \chi)$ and $\sinh\eta$; see Eq. (33). From Eqs. (A5), (A10), and (A14), the solution (36) is obtained.

The normalized flow velocities u_{P}, u_{Ca}, and u_{Cb} are defined by

$$u_{\mathrm{J}}(y; \tilde{k}, \chi) = \iiint \zeta_\rho^2 \sin\theta_\zeta \Phi_{\mathrm{J}}(y, \boldsymbol{\zeta}; \tilde{k}, \chi) E \mathrm{d}\zeta_\rho \mathrm{d}\theta_\zeta \mathrm{d}\zeta_z \quad (\mathrm{J} = \mathrm{P}, \mathrm{Ca}, \text{ or } \mathrm{Cb}). \tag{A21}$$

Similarly, the normalized shear stresses S_{P}, S_{Ca}, and S_{Cb} are defined by

$$S_{\mathrm{J}}(y; \tilde{k}, \chi) = 2\iiint \zeta_\rho^3 \cos\theta_\zeta \sin\theta_\zeta \Phi_{\mathrm{J}}(y, \boldsymbol{\zeta}; \tilde{k}, \chi) E \mathrm{d}\zeta_\rho \mathrm{d}\theta_\zeta \mathrm{d}\zeta_z \quad (\mathrm{J} = \mathrm{P}, \mathrm{Ca}, \text{ or } \mathrm{Cb}). \tag{A22}$$

The flow-rate coefficients m_{P}, m_{Ca}, and m_{Cb} are defined by

$$m_{\mathrm{J}}(\tilde{k}, \chi) = \gamma \int_0^1 H u_J(y; \tilde{k}, \chi) \mathrm{d}y \quad (\mathrm{J} = \mathrm{P}, \mathrm{Ca}, \text{ or } \mathrm{Cb}). \tag{A23}$$

Incidentally, for the BGKW kinetic model, the linearized collision integral is

$$\mathcal{L}(\Phi) = \iiint K(\boldsymbol{\zeta}, \boldsymbol{\zeta}_*)\Phi(\boldsymbol{\zeta}_*)\zeta_{\rho *} E_* \mathrm{d}\zeta_{\rho *} \mathrm{d}\theta_{\zeta *} \mathrm{d}\zeta_{z *} - \Phi,$$

$$K(\boldsymbol{\zeta}, \boldsymbol{\zeta}_*) = 1 + 2\zeta_\rho \zeta_{\rho *} \cos(\theta_\zeta - \theta_{\zeta *}) + 2\zeta_z \zeta_{z *} + \frac{2}{3}\left(\zeta_\rho^2 + \zeta_z^2 - \frac{3}{2}\right)\left(\zeta_{\rho *}^2 + \zeta_{z *}^2 - \frac{3}{2}\right), \tag{A24}$$

where $E_* = \pi^{-3/2}\exp(-\zeta_{\rho *}^2 - \zeta_{z *}^2)$. The data presented in Figs. 2 and 4 are computed by substituting Eq. (A24) into Eqs. (A15)–(A20) and solving numerically using a finite-difference method [11].

For the infinite Knudsen number ($\tilde{k} = \infty$), the solutions $\Phi_{\rm Ca}$ and $\Phi_{\rm Cb}$ are given by

$$\Phi_{\rm Ca} = \begin{cases} 2\zeta_\rho \sin\theta_\zeta \frac{\cosh\eta_a - \cos\chi}{\cosh\eta - \cos\chi} & [|\theta_\zeta| < \Theta(\eta,\chi)], \\ 0 & [|\theta_\zeta| > \Theta(\eta,\chi)], \end{cases} \tag{A25}$$

$$\Phi_{\rm Cb} = \begin{cases} 0 & [|\theta_\zeta| < \Theta(\eta,\chi)], \\ 2\zeta_\rho \sin\theta_\zeta \frac{\cosh\eta_b - \cos\chi}{\cosh\eta - \cos\chi} & [|\theta_\zeta| > \Theta(\eta,\chi)], \end{cases} \tag{A26}$$

where

$$\Theta(\eta,\chi) = \mathrm{Arcsin}\left(\frac{\cosh\eta - \cos\chi}{\cosh\eta_a - \cos\chi}\right), \tag{A27}$$

in terms of the original variable η. Therefore,

$$u_{\rm Ca} = \left[\frac{1}{2} - \Lambda(\eta,\chi)\right]\frac{\cosh\eta_a - \cos\chi}{\cosh\eta - \cos\chi}, \tag{A28}$$

$$u_{\rm Cb} = \left[\frac{1}{2} + \Lambda(\eta,\chi)\right]\frac{\cosh\eta_b - \cos\chi}{\cosh\eta - \cos\chi}, \tag{A29}$$

where

$$\Lambda(\eta,\chi) = \frac{\pi/2 - \Theta(\eta,\chi) + \sin 2\Theta(\eta,\chi)/2}{\pi}. \tag{A30}$$

From Eqs. (A28) and (A29), we find

$$u_{\rm Cb} - u_{\rm Ca} = O(\sqrt{c}), \tag{A31}$$

$$u_{\rm Cb} + u_{\rm Ca} = 1 + O(c), \tag{A32}$$

because $\eta_b - \eta_a = O(c)$ [see Eq. (8)] and $\Lambda = O(\sqrt{c})$ (see below). Multiplying both sides of Eq. (A31) by γH and integrating with respect to y, we obtain

$$m_{\rm Cb} - m_{\rm Ca} = O(\sqrt{c}). \tag{A33}$$

To derive $\Lambda = O(\sqrt{c})$, we used $\cos(\pi/2 - \Theta) = \sin\Theta = 1 - cqy + \cdots$ from Eq. (A27) where $q = -\gamma \sinh\eta_a/(\cosh\eta_a - \cos\chi) = O(1)$, and hence $\pi/2 - \Theta = (2cqy)^{1/2} + \cdots$.

APPENDIX B: REYNOLDS EQUATION BASED ON THE NAVIER–STOKES EQUATION

In this Appendix, the Reynolds equation is derived from the Navier–Stokes equation and the slip boundary condition. In this Appendix, we follow an approach that is more familiar in continuum tribology. To this end, we use the following dimensionless flow velocities:

$$u_\eta = \frac{v_\eta}{v_w}, \quad u_\chi = \frac{v_\chi}{v_w}, \tag{B1}$$

where $v_w = \max(|v_{wa}|, |v_{wb}|)$, in place of $\hat{v}_\eta$ and $\hat{v}_\eta$, because $u_\chi = O(1)$ is convenient in this analysis. We assume that the gas temperature is uniform because Eq. (36) yields $\hat{T} = 1$, then the viscosity of the gas is also uniform. We study the solution under the condition

$$c \ll k \ll 1, \quad \hat{v}_w = O(c), \tag{B2}$$

where $\hat{v}_w = v_w/(2RT_0)^{1/2}$ is a quantity of the order of the Mach number. The Reynolds number Re is, from Eq. (46),

$$\mathrm{Re} = \frac{\rho_0 v_w (r_b - r_a)}{\mu_0} = \frac{2\hat{v}_w}{\gamma_1 k}, \quad \text{thus} \quad c \ll \mathrm{Re} \ll 1. \tag{B3}$$

Our goal is to derive a Reynolds equation that is correct up to $O(c)$.

The dimensionless Navier–Stokes equation in the bipolar coordinate system in Fig. 1(b) is given by

$$\frac{\partial(H\hat{\rho}u_\eta)}{\partial y}+c\gamma\frac{\partial(H\hat{\rho}u_\chi)}{\partial\chi}=0, \tag{B4}$$

$$\hat{\rho}\left(\frac{u_\eta}{\gamma H}\frac{\partial u_\eta}{\partial y}+c\frac{u_\chi}{H}\frac{\partial u_\eta}{\partial\chi}-c\frac{\sinh\eta}{\sinh\eta_a}u_\chi^2+c\frac{\sin\chi}{\sinh\eta_a}u_\chi u_\eta\right)$$
$$=-\frac{1}{2\hat{v}_w^2\gamma H}\frac{\partial\hat{p}}{\partial y}+\frac{1}{\mathrm{Re}}\left[-\frac{1}{H}\frac{\partial}{\partial\chi}\left(\frac{c}{\gamma H^2}\frac{\partial Hu_\chi}{\partial y}-\frac{c^2}{H^2}\frac{\partial Hu_\eta}{\partial\chi}\right)+\frac{4}{3\gamma H}\frac{\partial\mathrm{div}\mathbf{u}}{\partial y}\right], \tag{B5}$$

$$\hat{\rho}\left(\frac{u_\eta}{\gamma H}\frac{\partial u_\chi}{\partial y}+c\frac{u_\chi}{H}\frac{\partial u_\chi}{\partial\chi}-c\frac{\sin\chi}{\sinh\eta_a}u_\eta^2+c\frac{\sinh\eta}{\sinh\eta_a}u_\chi u_\eta\right)$$
$$=-\frac{c}{2\hat{v}_w^2H}\frac{\partial\hat{p}}{\partial\chi}+\frac{1}{\mathrm{Re}}\left[\frac{1}{\gamma H}\frac{\partial}{\partial y}\left(\frac{1}{\gamma H^2}\frac{\partial Hu_\chi}{\partial y}-\frac{c}{H^2}\frac{\partial Hu_\eta}{\partial\chi}\right)+c\frac{4}{3H}\frac{\partial\mathrm{div}\mathbf{u}}{\partial\chi}\right], \tag{B6}$$

$$\hat{\rho}=\hat{p},\quad \mathrm{div}\mathbf{u}=\frac{1}{H^2}\left(\frac{1}{\gamma}\frac{\partial Hu_\eta}{\partial y}+c\frac{\partial Hu_\chi}{\partial\chi}\right). \tag{B7}$$

The factor $(2\hat{v}_w^2)^{-1}$ appears in the pressure-gradient terms in Eqs. (B5) and (B6) because we use the dimensionless pressure $\hat{p}=p/p_0$ here rather than $p/(\rho_0v_w^2)$. The slip boundary conditions are given by

$$u_\chi+\frac{k}{\hat{p}}\frac{k_0}{\gamma H_a}\frac{\partial u_\chi}{\partial y}=\frac{\hat{v}_{wa}}{\hat{v}_w},\quad u_\eta=0\quad(y=0), \tag{B8}$$

$$u_\chi-\frac{k}{\hat{p}}\frac{k_0}{\gamma H_b}\frac{\partial u_\chi}{\partial y}=\frac{\hat{v}_{wb}}{\hat{v}_w},\quad u_\eta=0\quad(y=1), \tag{B9}$$

where k_0 is the slip coefficient [3] which depends on the molecular model, e.g., $k_0=-1.016$ for the BGKW equation and the diffuse-reflection boundary condition, and H_a and H_b are H at $y=0$ and $y=1$, respectively. The dimensionless pressure $\hat{p}$, which is unknown, enters the boundary conditions (B8) and (B9) because the mean free path varies significantly due to the finite pressure variation. The normal and shear components of the stress are given by

$$\hat{p}_{\eta\eta}=\hat{p}-\frac{2\hat{v}_w^2}{\mathrm{Re}}\left(\frac{2}{\gamma H}\frac{\partial u_\eta}{\partial y}+2c\frac{\sin\chi}{\sinh\eta_a}u_\chi-\frac{2}{3}\mathrm{div}\mathbf{u}\right), \tag{B10}$$

$$\hat{p}_{\chi\eta}=-\frac{2\hat{v}_w^2}{\mathrm{Re}}\left(\frac{1}{\gamma H}\frac{\partial u_\chi}{\partial y}+\frac{c}{H}\frac{\partial u_\eta}{\partial\chi}-c\frac{\sin\chi}{\sinh\eta_a}u_\eta-c\frac{\sinh\eta}{\sinh\eta_a}u_\chi\right). \tag{B11}$$

From the boundary conditions (B8) and (B9), we find $u_\chi=O(1)$. Substituting this into the continuity equation (B4), we obtain

$$u_\eta=-\frac{c\gamma}{H\hat{\rho}}\int_0^y\frac{\partial(H\hat{\rho}u_\chi)}{\partial\chi}\mathrm{d}y=O(c). \tag{B12}$$

Thus, $\mathrm{div}\mathbf{u}=O(c)$. Multiplying both sides of Eq. (B5) by c, and noting that $(\sinh\eta_a)^{-1}\sinh\eta$ and $(\sinh\eta_a)^{-1}\sin\chi$ are of $O(1)$, we obtain

$$\frac{c\mathrm{Re}}{2\hat{v}_w^2}\frac{\partial\hat{p}}{\partial y}=O(c\mathrm{Re}). \tag{B13}$$

That is, $c\mathrm{Re}(2\hat{v}_w^2)^{-1}\hat{p}$ is independent of y up to $O(c)$. However, by neglecting the terms of $O(c\mathrm{Re})$ in Eq. (B6), we obtain

$$\frac{1}{\gamma H}\frac{\partial}{\partial y}\left(\frac{1}{\gamma H^2}\frac{\partial Hu_\chi}{\partial y}\right)=\frac{c\mathrm{Re}}{2\hat{v}_w^2H}\frac{\mathrm{d}\hat{p}}{\mathrm{d}\chi}. \tag{B14}$$

This equation can be further simplified by using $\partial H/\partial y = O(cH)$ and neglecting the term of $O(c^2)$, to yield

$$\frac{\partial^2 u_\chi}{\partial y^2} = \frac{c\gamma_1 \mathrm{Re}}{2\hat{v}_w^2}\frac{\gamma^2 H}{\gamma_1}\frac{\hat{p}}{k}\frac{k}{\hat{p}}\frac{\mathrm{d}\hat{p}}{\mathrm{d}\chi}. \tag{B15}$$

Equation (B15) and the boundary conditions (B8) and (B9) constitute the linear and inhomogeneous boundary-value problem to determine u_χ that is correct up to $O(c)$. Because of the linearity, the solution is given by

$$u_\chi = \frac{c\gamma_1 \mathrm{Re}}{2\hat{v}_w^2}\frac{k}{\hat{p}}\frac{\mathrm{d}\hat{p}}{\mathrm{d}\chi}u_{\mathrm{P}}^{\mathrm{ns}}\left(y;\frac{k}{\hat{p}},\chi\right) + \frac{\hat{v}_{wa}}{\hat{v}_w}u_{\mathrm{Ca}}^{\mathrm{ns}}\left(y;\frac{k}{\hat{p}},\chi\right) + \frac{\hat{v}_{wb}}{\hat{v}_w}u_{\mathrm{Cb}}^{\mathrm{ns}}\left(y;\frac{k}{\hat{p}},\chi\right). \tag{B16}$$

Here, $u_{\mathrm{P}}^{\mathrm{ns}}(y;\tilde{k},\chi)$, $u_{\mathrm{Ca}}^{\mathrm{ns}}(y;\tilde{k},\chi)$, and $u_{\mathrm{Cb}}^{\mathrm{ns}}(y;\tilde{k},\chi)$ are solutions of the following linear boundary-value problems: for $u_{\mathrm{P}}^{\mathrm{ns}}(y;\tilde{k},\chi)$ (Poiseuille flow),

$$\frac{\partial^2 u_{\mathrm{P}}^{\mathrm{ns}}}{\partial y^2} = \frac{\gamma^2}{\gamma_1\tilde{k}}H, \tag{B17}$$

$$u_{\mathrm{P}}^{\mathrm{ns}} - \beta_a\frac{\partial u_{\mathrm{P}}^{\mathrm{ns}}}{\partial y} = 0 \quad (y=0), \qquad u_{\mathrm{P}}^{\mathrm{ns}} + \beta_b\frac{\partial u_{\mathrm{P}}^{\mathrm{ns}}}{\partial y} = 0 \quad (y=1), \tag{B18}$$

for $u_{\mathrm{Ca}}^{\mathrm{ns}}(y;\tilde{k},\chi)$ (Couette flow for inner rotation),

$$\frac{\partial^2 u_{\mathrm{Ca}}^{\mathrm{ns}}}{\partial y^2} = 0, \tag{B19}$$

$$u_{\mathrm{Ca}}^{\mathrm{ns}} - \beta_a\frac{\partial u_{\mathrm{Ca}}^{\mathrm{ns}}}{\partial y} = 1 \quad (y=0), \qquad u_{\mathrm{Ca}}^{\mathrm{ns}} + \beta_b\frac{\partial u_{\mathrm{Ca}}^{\mathrm{ns}}}{\partial y} = 0 \quad (y=1), \tag{B20}$$

and for $u_{\mathrm{Cb}}^{\mathrm{ns}}(y;\tilde{k},\chi)$ (Couette flow for outer rotation),

$$\frac{\partial^2 u_{\mathrm{Cb}}^{\mathrm{ns}}}{\partial y^2} = 0, \tag{B21}$$

$$u_{\mathrm{Cb}}^{\mathrm{ns}} - \beta_a\frac{\partial u_{\mathrm{Cb}}^{\mathrm{ns}}}{\partial y} = 0 \quad (y=0), \qquad u_{\mathrm{Cb}}^{\mathrm{ns}} + \beta_b\frac{\partial u_{\mathrm{Cb}}^{\mathrm{ns}}}{\partial y} = 1 \quad (y=1), \tag{B22}$$

where

$$\beta_a = \frac{-k_0\tilde{k}}{\gamma H_a}, \qquad \beta_b = \frac{-k_0\tilde{k}}{\gamma H_b}. \tag{B23}$$

As in Sec. III B, the solution (B16) is undetermined unless $\hat{p}(\chi)$ is known.

The dimensionless pressure $\hat{p}$ is determined by the mass conservation Eq. (31), which can also be obtained by evaluating Eq. (B12) at $y=1$ and multiplying by $\hat{v}_w$. From Eqs. (B16) and (B3), we obtain $\hat{v}_\chi(=\hat{v}_w u_\chi)$ as

$$\hat{v}_\chi = c\left[\frac{1}{\hat{p}}\frac{\mathrm{d}\hat{p}}{\mathrm{d}\chi}u_{\mathrm{P}}^{\mathrm{ns}}\left(y;\frac{k}{\hat{p}},\chi\right) + \frac{\hat{v}_{wa}}{c}u_{\mathrm{Ca}}^{\mathrm{ns}}\left(y;\frac{k}{\hat{p}},\chi\right) + \frac{\hat{v}_{wb}}{c}u_{\mathrm{Cb}}^{\mathrm{ns}}\left(y;\frac{k}{\hat{p}},\chi\right)\right]. \tag{B24}$$

Substituting Eq. (B24) into Eq. (31), we obtain

$$\frac{\mathrm{d}}{\mathrm{d}\chi}\left[m_{\mathrm{P}}^{\mathrm{ns}}\left(\frac{k}{\hat{p}},\chi\right)\frac{\mathrm{d}\hat{p}}{\mathrm{d}\chi} + u_{wa}\hat{p}m_{\mathrm{Ca}}^{\mathrm{ns}}\left(\frac{k}{\hat{p}},\chi\right) + u_{wb}\hat{p}m_{\mathrm{Cb}}^{\mathrm{ns}}\left(\frac{k}{\hat{p}},\chi\right)\right] = 0, \tag{B25}$$

where $m_{\mathrm{P}}^{\mathrm{ns}}(\tilde{k},\chi)$, $m_{\mathrm{Ca}}^{\mathrm{ns}}(\tilde{k},\chi)$, and $m_{\mathrm{Cb}}^{\mathrm{ns}}(\tilde{k},\chi)$ are defined by

$$m_{\mathrm{J}}^{\mathrm{ns}} = \gamma\int_0^1 H u_{\mathrm{J}}^{\mathrm{ns}}\mathrm{d}y \quad (\mathrm{J} = \mathrm{P},\ \mathrm{Ca},\ \text{or}\ \mathrm{Cb}). \tag{B26}$$

Equation (B25) is the Reynolds equation derived from the Navier–Stokes equation and the slip boundary condition. Equation (B25) is of the same form as Eq. (37) in Sec. III B except that the flow-rate coefficients $m_{\rm P}$, $m_{\rm Ca}$, and $m_{\rm Cb}$ in the latter are replaced by $m_{\rm P}^{\rm ns}$, $m_{\rm Ca}^{\rm ns}$, and $m_{\rm Cb}^{\rm ns}$, respectively. The process to construct the solution is similar to that in Sec. III B. The flow-rate coefficients in Eq. (B25) contain $\hat{p}$ through the first argument $k/\hat{p}$, which originates from the $k/\hat{p}$ dependence of the slip factors in Eqs. (B8) and (B9). The components of the stress that are correct up to $O(c)$ are

$$\hat{p}_{\eta\eta} = \hat{p}, \tag{B27}$$

$$\hat{p}_{\chi\eta} = c\left[\frac{{\rm d}\hat{p}}{{\rm d}\chi} S_{\rm P}^{\rm ns}\left(y; \frac{k}{\hat{p}}, \chi\right) + u_{wa}\hat{p} S_{\rm Ca}^{\rm ns}\left(y; \frac{k}{\hat{p}}, \chi\right) + u_{wb}\hat{p} S_{\rm Cb}^{\rm ns}\left(y; \frac{k}{\hat{p}}, \chi\right)\right], \tag{B28}$$

where $S_{\rm P}^{\rm ns}(y; \tilde{k}, \chi)$, $S_{\rm Ca}^{\rm ns}(y; \tilde{k}, \chi)$, and $S_{\rm Cb}^{\rm ns}(y; \tilde{k}, \chi)$ are to be given by Eqs. (B32) and (B33) below.

Our final task is to solve Eqs. (B17)–(B22) to obtain the coefficients $m_{\rm P}^{\rm ns}$, $m_{\rm Ca}^{\rm ns}$, and $m_{\rm Cb}^{\rm ns}$. Because we are interested in the solution that is correct up to $O(c)$, the Taylor expansion $H = H_a(1 + c\gamma H_a y)$ of the scale factor H may be used. Then, Eqs. (B17)–(B22) are integrated analytically to yield

$$u_{\rm P}^{\rm ns} = -\frac{\gamma^2 H_a}{2\gamma_1 \tilde{k}}\left\{\frac{1+2\beta_b}{1+\beta_a+\beta_b}(y+\beta_a) - y^2 + c\frac{\gamma H_a}{3}\left[\frac{1+3\beta_b}{1+\beta_a+\beta_b}(y+\beta_a) - y^3\right]\right\}, \tag{B29}$$

$$u_{\rm Ca}^{\rm ns} = \frac{1+\beta_b-y}{1+\beta_a+\beta_b}, \tag{B30}$$

$$u_{\rm Cb}^{\rm ns} = \frac{\beta_a+y}{1+\beta_a+\beta_b}, \tag{B31}$$

$$S_{\rm P}^{\rm ns} = \frac{\gamma H_a}{2H}\left[\frac{1+2\beta_b}{1+\beta_a+\beta_b} - 2y + c\frac{\gamma H_a}{3}\left(\frac{1+3\beta_b}{1+\beta_a+\beta_b} - 3y^2\right)\right], \tag{B32}$$

$$S_{\rm Ca}^{\rm ns} = -S_{\rm Cb}^{\rm ns} = \frac{\gamma_1 \tilde{k}}{\gamma H}\frac{1}{1+\beta_a+\beta_b}, \tag{B33}$$

where β_a and β_b are defined by Eq. (B23). Substituting Eqs. (B29)–(B31) into Eqs. (B26), we obtain

$$m_{\rm P}^{\rm ns} = -\frac{\gamma^3 H_a^2}{12\gamma_1 \tilde{k}}\frac{1+4\beta_a+4\beta_b+12\beta_a\beta_b + c\gamma H_a(1+3\beta_a+5\beta_b+12\beta_a\beta_b)}{1+\beta_a+\beta_b}, \tag{B34}$$

$$m_{\rm Ca}^{\rm ns} = \frac{\gamma H_a}{2}\frac{1+2\beta_b}{1+\beta_a+\beta_b}\left(1 + c\frac{\gamma H_a}{3}\frac{1+3\beta_b}{1+2\beta_b}\right), \tag{B35}$$

$$m_{\rm Cb}^{\rm ns} = \frac{\gamma H_a}{2}\frac{1+2\beta_a}{1+\beta_a+\beta_b}\left(1 + c\frac{\gamma H_a}{3}\frac{2+3\beta_a}{1+2\beta_a}\right). \tag{B36}$$

The nonslip solution is obtained by putting $\beta_a = \beta_b = 0$.

From Eqs. (B35) and (B36), we find

$$m_{\rm Cb}^{\rm ns} - m_{\rm Ca}^{\rm ns} = c\frac{(\gamma H_a)^2}{6}\frac{1+6\beta_a}{1+\beta_a+\beta_b} > 0, \tag{B37}$$

neglecting the terms of $O(c^2)$, that is, the difference in the flow-rate coefficients of Couette flows between the outer and inner rotations is of $O(c)$. From Eqs. (B30) and (B31) we find

$$u_{\rm Cb}^{\rm ns} + u_{\rm Ca}^{\rm ns} = 1, \tag{B38}$$

that is, the sum of the normalized flow velocities $u_{\rm Ca}^{\rm ns}$ and $u_{\rm Cb}^{\rm ns}$ of the two Couette flows is unity when neglecting the terms of $O(c^2)$. Equations (B37) and (B38) play important roles in Secs. III B and V.

APPENDIX C: DATABASE OF THE FUNCTIONS $m_{\rm Ca}$ AND $m_{\rm Cb}$

A simple database of the functions $m_{\rm Ca}(\tilde{k}, \chi)$ and $m_{\rm Cb}(\tilde{k}, \chi)$ [Eq. (A23)] is provided here. This database is based on Chebyshev interpolation for two independent variables $\tilde{k}$ and χ, and is a

TABLE I. Coefficients $C_{\mathrm{Ca}mn}$ and $C_{\mathrm{Cb}mn}$ in Eq. (C1) for $c = 0.025$ and $\varepsilon = 0.5$ (BGKW model).

	m	$n=0$	1	2	3	4	5	6
$C_{\mathrm{Ca}mn}$	0	−0.94788	0.60092	0.06891	−0.06200	−0.01941	−0.00291	0.00049
	1	−0.07354	−0.01801	−0.00281	0.00166	0.00076	0.00018	−0.00001
	2	−0.02127	−0.00808	−0.00135	0.00071	0.00037	0.00009	0.00000
	3	0.00210	−0.00148	−0.00033	0.00011	0.00009	0.00002	0.00001
	4	0.00384	0.00072	0.00005	−0.00008	−0.00002	0.00000	0.00000
	5	0.00084	0.00067	0.00009	−0.00007	−0.00003	0.00000	0.00000
	6	−0.00044	0.00012	0.00004	−0.00001	−0.00001	0.00000	0.00000
	7	−0.00033	−0.00012	0.00000	0.00001	0.00000	0.00000	0.00000
$C_{\mathrm{Cb}mn}$	0	−0.83728	0.62540	0.07279	−0.06423	−0.02045	−0.00318	0.00050
	1	0.06290	0.01257	0.00165	−0.00126	−0.00047	−0.00008	0.00002
	2	0.01649	0.00538	0.00076	−0.00052	−0.00022	−0.00004	0.00000
	3	−0.00285	0.00079	0.00016	−0.00006	−0.00005	−0.00001	0.00000
	4	−0.00334	−0.00062	−0.00004	0.00007	0.00001	0.00000	0.00000
	5	−0.00048	−0.00047	−0.00006	0.00005	0.00002	0.00000	0.00000
	6	0.00048	−0.00005	−0.00002	0.00000	0.00001	0.00000	0.00000
	7	0.00027	0.00011	0.00000	−0.00001	0.00000	0.00000	0.00000

straightforward application of that in Ref. [13]. The formula for $m_{\mathrm{J}}(\tilde{k}, \chi)$ (J = Ca or Cb) that is valid in the domain $0.05 \leqslant \tilde{k} \leqslant 20$ and $0 \leqslant \chi \leqslant 2\pi$ is given by

$$m_{\mathrm{J}}(\tilde{k}, \chi) = \exp\left[\sum_{m=0}^{N_m-1}\sum_{n=0}^{N_n-1} C_{\mathrm{J}mn} T_m(A \ln \tilde{k}) T_n(2|\chi/\pi - 1| - 1)\right] \quad (\mathrm{J} = \mathrm{Ca\ or\ Cb}), \tag{C1}$$

where $A = 1/(\ln 20)$. The N_m and N_n are constants that are chosen appropriately, and $C_{\mathrm{J}mn}$ are constants determined by c and ε, and a choice of N_m and N_n. For $c = 0.025$ and $\varepsilon = 0.5$, for example, $N_m = 8, N_n = 7$, and the values of $C_{\mathrm{Ca}mn}$ and $C_{\mathrm{Cb}mn}$ are presented in Table I. Values for other c and ε are available from Ref. [19]. Equation (C1) is also applicable to the function m_{P} provided that the coefficients $C_{\mathrm{P}mn}$ in Ref. [19] is used and that the right-hand side is multiplied by -1. The functions $T_n(\cdot)$'s are the Chebyshev polynomials defined by $T_0(t) = 1, T_1(t) = t$, and $T_n(t) = 2tT_{n-1}(t) - T_{n-2}(t)$ $(n = 2, 3, \cdots)$. A comparison with the results of direct calculations of Eq. (A23) shows that the approximation error of Eq. (C1) using Table I is uniformly less than 0.1% in the domain $0.05 \leqslant \tilde{k} \leqslant 20$ and $0 \leqslant \chi \leqslant 2\pi$.

APPENDIX D: DERIVATION OF THE WOC MODEL

In this Appendix, the WOC model of the lubrication equation is derived. The derivation is quite similar to both that in Appendix A and that in Appendix E in Ref. [11], and so it is outlined only briefly here. The basic equations are Eqs. (23)–(29). Now Eq. (34) is replaced by the original form (23) without using $\mathrm{D}'_{\mathrm{ec}}$. The solution $\hat{f}$ is sought in the form of the power-series expansion (32), in which the second and third terms on the left-hand side of Eq. (23) are now treated as higher-order terms because of the small factor c.

Substituting the expansion (32) into Eqs. (23)–(29) and formally arranging terms of the same order in c, the boundary-value problem for the leading-order solution $\hat{f}_{(0)}$ is

$$\frac{\zeta_\rho \cos\theta_\zeta}{\gamma H}\frac{\partial \hat{f}_{(0)}}{\partial y} = \frac{1}{k}\hat{J}(\hat{f}_{(0)}, \hat{f}_{(0)}), \tag{D1}$$

together with Eqs. (A2)–(A4). The only difference from Appendix A is that the operator $\mathrm{D}'_{\mathrm{ec}}$ is replaced by its first term $(\gamma H)^{-1}\cos\theta_\zeta\,\partial/\partial y$ alone. A solution $\hat{f}_{(0)}$ is an equilibrium state (A5) at rest.

The boundary-value problem for the first-order solution $\hat{f}_{(1)}$ is

$$\frac{\zeta_\rho\cos\theta_\zeta}{\gamma H}\frac{\partial\hat{f}_{(1)}}{\partial y}=\frac{2}{k}\hat{J}(\hat{f}_{(0)},\hat{f}_{(1)})-\frac{\zeta_\rho\sin\theta_\zeta}{H}\frac{\partial\hat{f}_{(0)}}{\partial\chi}, \tag{D2}$$

together with Eqs. (A7)–(A9). Once more, the only difference from Appendix A is that the operator $\mathrm{D}'_{\mathrm{ec}}$ is replaced by its first term alone. The curvature term $\zeta_\rho G\partial\hat{f}_{(0)}/\partial\theta_\zeta$, which ought to appear as an inhomogeneous term, vanishes because the leading-order solution (A5) is independent of θ_ζ. The solution $\hat{f}_{(1)}$ can be sought following a quite similar way to that in Appendix A, from which we obtain

$$\begin{aligned}\hat{f}(y,\chi,\boldsymbol{\zeta})=\hat{p}_{(0)}E\Bigg\{1+c\Bigg[&\frac{1}{\hat{p}_{(0)}}\frac{\mathrm{d}\hat{p}_{(0)}}{\mathrm{d}\chi}\Phi_{\mathrm{P}}^{\mathrm{woc}}\left(y,\boldsymbol{\zeta};\frac{k}{\hat{p}_{(0)}},\chi\right)\\&+u_{wa}\Phi_{\mathrm{Ca}}^{\mathrm{woc}}\left(y,\boldsymbol{\zeta};\frac{k}{\hat{p}_{(0)}},\chi\right)+u_{wb}\Phi_{\mathrm{Cb}}^{\mathrm{woc}}\left(y,\boldsymbol{\zeta};\frac{k}{\hat{p}_{(0)}},\chi\right)+\frac{C_{(1)}}{\hat{p}_{(0)}}\Bigg]\Bigg\},\end{aligned} \tag{D3}$$

which is the counterpart of Eq. (36). The functions $\Phi_{\mathrm{P}}^{\mathrm{woc}}(y,\boldsymbol{\zeta};\tilde{k},\chi)$, $\Phi_{\mathrm{Ca}}^{\mathrm{woc}}(y,\boldsymbol{\zeta};\tilde{k},\chi)$, and $\Phi_{\mathrm{Cb}}^{\mathrm{woc}}(y,\boldsymbol{\zeta};\tilde{k},\chi)$ are the solutions of the same boundary-value problems as Eqs. (A15)–(A16), Eqs. (A17)–(A18), and Eqs. (A19)–(A20), respectively, except that the operator $\mathrm{D}'_{\mathrm{ec}}$ is replaced by its first term alone. For example, for $\Phi_{\mathrm{Ca}}^{\mathrm{woc}}$ (Couette flow for inner rotation),

$$\frac{\zeta_\rho\cos\theta_\zeta}{\gamma H}\frac{\partial\Phi_{\mathrm{Ca}}^{\mathrm{woc}}}{\partial y}=\frac{1}{\tilde{k}}\mathcal{L}\big(\Phi_{\mathrm{Ca}}^{\mathrm{woc}}\big), \tag{D4}$$

$$\Phi_{\mathrm{Ca}}^{\mathrm{woc}}=2\zeta_\rho\sin\theta_\zeta\ (y=0,\ \cos\theta_\zeta>0),\quad \Phi_{\mathrm{Ca}}^{\mathrm{woc}}=0\ (y=1,\ \cos\theta_\zeta<0), \tag{D5}$$

and for $\Phi_{\mathrm{Cb}}^{\mathrm{woc}}$ (Couette flow for outer rotation),

$$\frac{\zeta_\rho\cos\theta_\zeta}{\gamma H}\frac{\partial\Phi_{\mathrm{Cb}}^{\mathrm{woc}}}{\partial y}=\frac{1}{\tilde{k}}\mathcal{L}\big(\Phi_{\mathrm{Cb}}^{\mathrm{woc}}\big), \tag{D6}$$

$$\Phi_{\mathrm{Cb}}^{\mathrm{woc}}=0\ (y=0,\ \cos\theta_\zeta>0),\quad \Phi_{\mathrm{Cb}}^{\mathrm{woc}}=2\zeta_\rho\sin\theta_\zeta\ (y=1,\cos\theta_\zeta<0). \tag{D7}$$

Substituting the distribution function (D3) into Eq. (30c) and then into Eq. (31), we obtain the Reynolds-type Eq. (42), which is the counterpart of Eq. (37). The flow-rate coefficients $m_{\mathrm{P}}^{\mathrm{woc}}$, $m_{\mathrm{Ca}}^{\mathrm{woc}}$, and $m_{\mathrm{Cb}}^{\mathrm{woc}}$ are given by Eqs. (A21) and (A23) in which Φ_{J} (J = P, Ca, or Cb) is replaced by $\Phi_{\mathrm{J}}^{\mathrm{woc}}$. The macroscopic variables are obtained in a similar manner to that in Appendix A. For example, the components of the stress are $\hat{p}_{\eta\eta}=\hat{p}$ and

$$\hat{p}_{\chi\eta}=c\left[\frac{\mathrm{d}\hat{p}_{(0)}}{\mathrm{d}\chi}S_{\mathrm{P}}^{\mathrm{woc}}\left(y;\frac{k}{\hat{p}_{(0)}},\chi\right)+u_{wa}\hat{p}_{(0)}S_{\mathrm{Ca}}^{\mathrm{woc}}\left(y;\frac{k}{\hat{p}_{(0)}},\chi\right)+u_{wb}\hat{p}_{(0)}S_{\mathrm{Cb}}^{\mathrm{woc}}\left(y;\frac{k}{\hat{p}_{(0)}},\chi\right)\right], \tag{D8}$$

where $S_{\mathrm{P}}^{\mathrm{woc}}$ is given by Eq. (A22) in which Φ_{P} is replaced by $\Phi_{\mathrm{P}}^{\mathrm{woc}}$, and so on.

Finally, Eqs. (43) and (44) are derived. To this end, we change the variables $(\zeta_\rho,\theta_\zeta,\zeta_z)$ to the original variables $(\zeta_\eta,\zeta_\chi,\zeta_z)$ by Eq. (22) and y to Y defined by

$$\mathrm{d}Y=\gamma H\mathrm{d}y,\quad Y=0\quad\text{at } y=0,\quad Y_1=\int_0^1\gamma H\mathrm{d}y. \tag{D9}$$

Here, Y and Y_1 depend on χ through H. The boundary-value problem (D4) and (D5) and that (D6) and (D7) are transformed into, respectively,

$$\zeta_\eta\frac{\partial\Phi_{\mathrm{Ca}}^{\mathrm{woc}}}{\partial Y}=\frac{1}{\tilde{k}}\mathcal{L}\big(\Phi_{\mathrm{Ca}}^{\mathrm{woc}}\big), \tag{D10}$$

$$\Phi_{\rm Ca}^{\rm woc} = 2\zeta_\chi \quad (Y = 0,\ \zeta_\eta > 0), \qquad \Phi_{\rm Ca}^{\rm woc} = 0 \quad (Y = Y_1,\ \zeta_\eta < 0), \tag{D11}$$

and

$$\zeta_\eta \frac{\partial \Phi_{\rm Cb}^{\rm woc}}{\partial Y} = \frac{1}{\tilde{k}} \mathcal{L}\big(\Phi_{\rm Cb}^{\rm woc}\big), \tag{D12}$$

$$\Phi_{\rm Cb}^{\rm woc} = 0 \quad (Y = 0,\ \zeta_\eta < 0), \qquad \Phi_{\rm Cb}^{\rm woc} = 2\zeta_\chi \quad (Y = Y_1,\ \zeta_\eta > 0). \tag{D13}$$

Regarding Y as the spatial variable, each problem is equivalent to that of *plane* Couette flow between the parallel planes ($0 < Y < Y_1$) in which either of the walls moves at the unit speed. As is well known, the flow rate is equal to $Y_1/2$, i.e.,

$$\int_0^{Y_1} {\rm d}Y \int \zeta_\chi \Phi_{\rm Ca}^{\rm woc} E \mathbf{d}\boldsymbol{\zeta} = \int_0^{Y_1} {\rm d}Y \int \zeta_\chi \Phi_{\rm Cb}^{\rm woc} E \mathbf{d}\boldsymbol{\zeta} = \frac{1}{2} Y_1. \tag{D14}$$

Using Eqs. (D9) and (22), we find

$$m_{\rm Ca}^{\rm woc} = m_{\rm Cb}^{\rm woc} = \tfrac{1}{2} Y_1. \tag{D15}$$

Thus, Eq. (43) is derived. Furthermore, Y_1 is independent of $\tilde{k}$ by definition (D9), and so $m_{\rm Ca}^{\rm woc}$ and $m_{\rm Cb}^{\rm woc}$ are independent of $\tilde{k}$, to yield Eq. (44). Relation (D15) is numerically confirmed. Similar to Eq. (D15), we can also show that $S_{\rm Ca}^{\rm woc} = -S_{\rm Cb}^{\rm woc}$.

[1] O. Reynolds, On the theory of lubrication and its application to Mr. Beauchamp Tower's experiments, including an experimental determination of the viscosity of olive oil, Philos. Trans. R. Soc. London, Ser. A **177**, 157 (1886).

[2] H. G. Elrod, A derivation of the basic equations for hydrodynamic lubrication with a fluid having constant properties, Quart. Appl. Math. **17**, 349 (1960).

[3] Y. Sone, *Molecular Gas Dynamics* (Birkhaüser, Boston, MA, 2007), Secs. 3.1 and 4.3.

[4] A. Burgdorfer, The influence of the molecular mean free path on the performance of hydrodynamic gas lubricated bearings, ASME J. Basic Eng. **81**, 94 (1959).

[5] R. F. Gans, Lubrication theory at arbitrary Knudsen number, ASME J. Tribol. **107**, 431 (1985).

[6] S. Fukui and R. Kaneko, Analysis of ultra-thin gas film lubrication based on linearized Boltzmann equation: First report—Derivation of a generalized lubrication equation including thermal creep flow, ASME J. Tribol. **110**, 253 (1988).

[7] T. Veijola, H. Kuisma, and J. Lahdenperä, The influence of gas-surface interaction on gas-film damping in a silicon accelerometer, Sens. Actuators A **66**, 83 (1998).

[8] G. Karniadakis, A. Beskok, and N. Aluru, *Microflows and Nanoflows: Fundamentals and Simulation* (Springer, New York, NY, 2005).

[9] C. Cercignani, *Slow Rarefied Flows* (Birkhaüser, Boston, MA, 2006).

[10] T. Doi, Effect of a small curvature of the surfaces on microscale lubrication of a gas for large Knudsen numbers, Phys. Rev. Fluids **7**, 034201 (2022).

[11] T. Doi, Generalized Reynolds equation for microscale lubrication between eccentric circular cylinders based on kinetic theory, J. Fluid Mech. **974**, A13 (2023).

[12] T. Doi, A model of micro lubrication between two walls with an arbitrary temperature difference based on kinetic theory, Phys. Fluids **32**, 052005 (2020).

[13] T. Doi, A model of micro lubrication between two walls with unequal temperature distribution based on kinetic theory, Phys. Fluids **33**, 032014 (2021).

[14] T. Doi, Kinetic theory analysis of microscale lubrication of a gas between eccentric circular cylinders with an arbitrary temperature difference, Phys. Fluids **36**, 042016 (2024).

[15] P. L. Bhatnagar, E. P. Gross, and M. Krook, A model for collision processes in gases. I. Small amplitude processes in charged and neutral one-component systems, Phys. Rev. **94**, 511 (1954).
[16] P. Welander, On the temperature jump in a rarefied gas, Ark. Fys. **7**, 507 (1954).
[17] Y. Wu, L. Yang, T. Xu, and W. Wu, Thermo-elasto-hydrodynamic characteristics analysis of journal microbearing lubricated with rarefied gas, Micromachines **11**, 955 (2020).
[18] M. Kogan, *Rarefied Gas Dynamics* (Plenum Press, New York, NY, 1969).
[19] T. Doi, Kinetic theory analysis of microscale lubrication of a gas between eccentric circular cylinders: Effect of rotation of the outer cylinder: SUPPLEMENTS, https://www.damp.tottori-u.ac.jp/∼lab9/.
[20] C. K. Chu, Kinetic-theoretic description of the formation of a shock wave, Phys. Fluids **8**, 12 (1965).
[21] H. Sugimoto and Y. Sone, Numerical analysis of steady flows of a gas evaporating from its cylindrical condensed phase on the basis of kinetic theory, Phys. Fluids A **4**, 419 (1992).
[22] T. Doi, Flows of a rarefied gas between coaxial circular cylinders with nonuniform surface properties, Open J. Fluid Dyn. **9**, 22 (2019).